Far-Infrared Optical Properties of V and Cr doped Sb_2Te_3

by

Anthony Madubuonu

A THESIS SUBMITTED IN PARTIAL FULFILMENT OF
THE REQUIREMENTS FOR THE DEGREE OF

MASTER OF SCIENCE

in

The Faculty of Mathematics and Sciences

Department of Physics

BROCK UNIVERSITY

October 3, 2008

Abstract

The far infrared reflectance of Sb_2Te_3, $Sb_{1.97}V_{0.03}Te_3$ and $Sb_{1.94}Cr_{0.06}Te_3$ was measured near normal incidence at different temperatures (between 45K and 300K). The direct current resistivities of the above samples were also measured between the temperatures of 4K and 300K. Also Kramers Kronig (KK) analyses were performed on the reflectance spectra to obtain the optical conductivities. In the doped samples, it was observed that a phonon at $62cm^{-1}$ softens to about $55cm^{-1}$ on decreasing the temperature from 295K to 45K. Also, it was observed that the plasma frequency of the doped samples is independent of doping. The scattering rate for the vanadium doped sample was seen to be greater than that for the chromium doped sample despite the fact that vanadium impurity density is less than that of chromium. The Drude-Lorentz model fits to the KK optical conductivity show that the samples used in this work are conventional metals. Definitive measurements of the temperature dependence of the scattering rate across the ferromagnetic transition await equipment changes allowing measurements at low temperature using the mercury cadmium telluride (MCT) detector.

Contents

List of Tables

List of Figures

Acknowledgements

I wish to thank my supervisor, Dr D. A. Crandles for his guidance and support throughout the duration of this work. Also, my gratitude goes to the members of the supervisory committee , Dr M. Reedyk, Dr S. Bose and Dr E. Sternin for their guidance. Dr C. Uher and Dr P. Lošt'ák deserve my appreciation for providing the samples used in this work. I am indebted to Steve and co. in the machine shop who helped in the design and construction of the system used in this work. I would like to thank Lee, BaoChang, Mojtaba, Patrick, Nick and everyone that contribute towards the successful completion of this work. Thanks to everyone in Physics department. Finally, I wish to express my gratitude to my friends Ifeanyi, Innocent and Philip. They are like members of my family in Canada.

Chapter 1

Introduction

1.1 Spintronics and DMS materials

Spintronics is a developing technology that harnesses the spin and the charge degrees of freedom of the electron, while conventional electronics exploits only the charge degree of freedom of the electron in the production of electronic devices. These spintronic devices when used in conjunction with charge-based electronic devices have the potential to consume less power and increase the speed of data processing [1].

Dilute magnetic semiconductors (DMS) are usually III-V or II-VI semiconductors, doped with small percentages (1-7%) of a transition metal atom. Interestingly, ferromagnetic behavior at room temperature has been observed in $Ti_{1-x}Co_xO_{2-\delta}(0\leq x\leq 0.02, \delta \ll 1)$ thin films. However, there are arguments as to whether this is true DMS behaviour or whether the ferromagnetic behaviour is due to Co clusters [2]. III-V DMS are ferromagnetic and could qualify for use in spintronics applications but the fact that the Curie temperatures of these DMS are generally much less than room temperature is a threat to this application [3, 4]. It is hoped that this study which will consider DMS materials based on Sb_2Te_3 will contribute to understanding the mechanism of DMS.

1.2 Antimony Telluride (Sb_2Te_3),vanadium doped Sb_2Te_3 and chromium doped Sb_2Te_3

Antimony telluride (Sb_2Te_3) has a tetradymite layered structure and is diamagnetic. The atomic layers are arranged in the sequence Te^2-Sb-Te^1-Sb-Te^2, perpendicular to the c axis, with the Te^1 atoms in the octahedral holes of the Sb atoms (Figure 1.1). Its primitive unit cell is trigonal. The bonding within the layers of Sb_2Te_3 is mixed covalent and ionic while
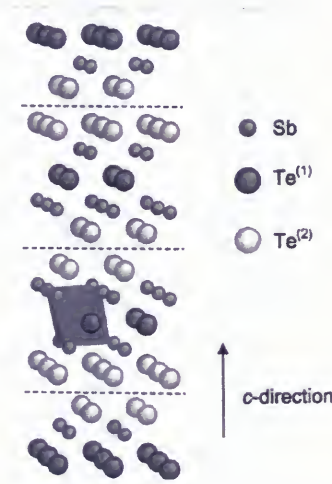
Figure 1.1: Crystal structure of Sb_2Te_3[3].

that between the layers (along the c-axis) is Van der Waals [3], thus the crystals cleave easily perpendicular to the c axis. The superscript depicts the kind of bonding that the Te atoms have with the Sb atoms in the lattice. Te^2 atoms are bound to the Sb atoms by mixed covalent and ionic bonds, while weak Van der Waals bonds connect Te^2 atoms with the Te^2 atoms of the adjacent five-layer unit. The Sb-Te^1 bond is weaker than the Te^2-Sb bond since it is less ionic. Sb_2Te_3 is a p-type semiconductor due to anti-site defects (the presence of Te(Sb) in Sb(Te) lattice) [3] resulting in a large number of holes (i.e $10^{22}cm^{-3}$). Since there are Te^1 and Te^2 sites, Sb could substitute any of the two. Hence in total, there are three kinds of anti-site defects (Figure 1.2) [5] that could occur in a Sb_2Te_3 crystal.

Sb$_2$Te$_3$ is also of potential value for use in thermoelectric cooling devices [3]. The anti-site defects produce a degenerate Fermi gas in Sb$_2$Te$_3$ with resistivity that increases with temperature and a Hall coefficient [3] that is approximately independent of temperature. Sb$_{2-x}$V$_x$Te$_3$(0.01≤x≤0.03) and Sb$_{2-x}$Cr$_x$Te$_3$ (0.01≤x≤0.095) are DMS formed by doping
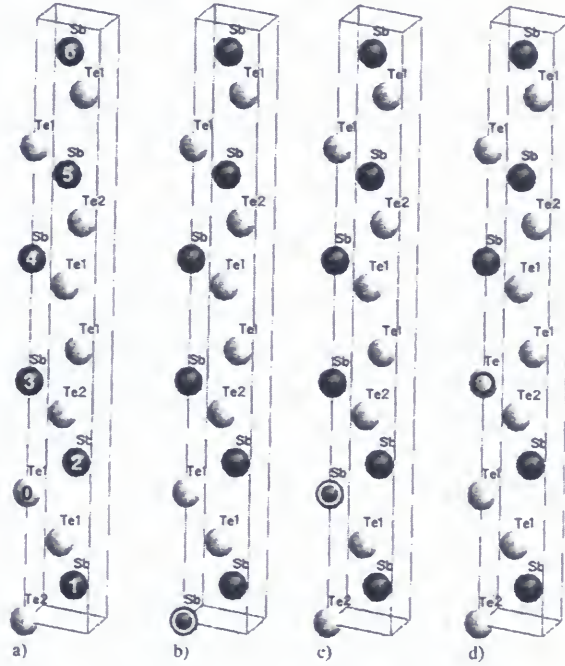
Figure 1.2: Unit cells of Sb$_2$Te$_3$ depicting the anti-site defects.(a) Unit cell with no defects showing six possibilities for the exchange of the Te atom marked 0 with Sb atoms marked 1-6.(b) Anti-site defect showing Sb in Te^2 site. (c) Anti-site defect showing Sb in Te^1 site.(d) Anti-site defect showing Te in Sb site [5]

Sb$_2$Te$_3$ with small concentrations of vanadium and chromium respectively, with Curie temperatures increasing with the doping concentration. The doped materials have negligible change (compared to Sb$_2$Te$_3$) in carrier concentration, while the in-plane electrical resistivities increase as shown in Figures 1.3b and 1.4 [3, 4]. Dyck confirmed the existence of ferromagnetism in the doped samples, but the coercive field (H$_C$=1.2 T) for magnetic field $\vec{B}$ measured parallel to c axis of the vanadium doped (Figure 1.5) sample is much greater than that of the chromium doped sample (H$_C$=0.015T), indicating that the mechanism of domain structure and magnetic order could differ in both materials [4].
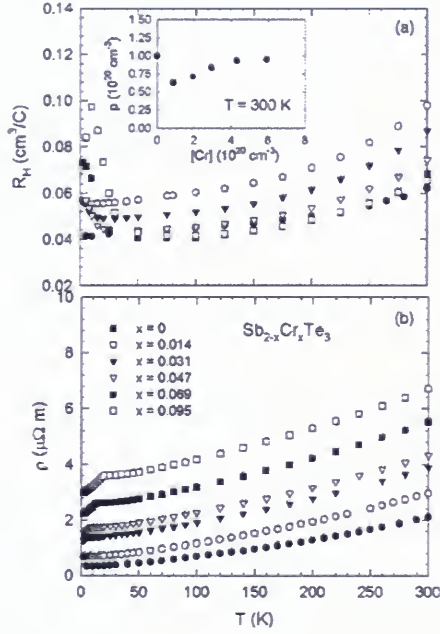
Figure 1.3: Variation of (a) Hall coefficient and (b) in-plane resistivity as a function of temperature for $Sb_{2-x}Cr_xTe_3$ ($0 \leq$ x ≤ 0.095) [4]. Hall Coefficient will be discussed in section 3.2. Inset in (a) shows hole concentration as a function of Cr doping.
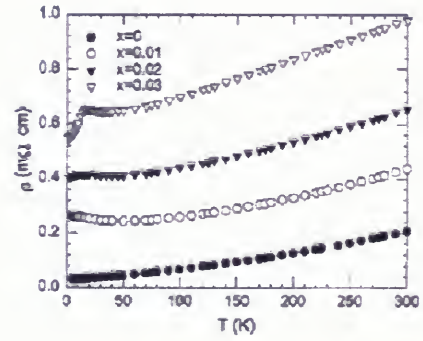
Figure 1.4: Temperature dependence of in-plane resistivity of $Sb_{2-x}V_xTe_3$ $Sb_{2-x}V_xTe_3$ ($0 \leq$ x ≤ 0.03). Observe that transition temperature (T_C) and ρ increase with doping concentration [3].
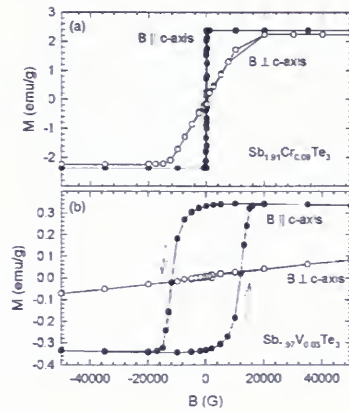
Figure 1.5: Juxtaposition of the hysteresis loop in $Sb_{2-x}Cr_xTe_3$ and $Sb_{2-x}V_xTe_3$ with magnetic field applied parallel and perpendicular to the c axis. The data was taken at 2K [4].

Lostak et. al. [6] showed that doping of Sb_2Te_3 with chromium does not significantly change the concentration of holes. The reason is that chromium impurities in the Sb_2Te_3 crystal give rise to two processes that compensate each other; substitution of Cr or V atoms for Sb atoms results in an increase in hole concentration and simultaneous reduction in the likelihood of formation of anti-site defects. Addition of Cr or V to the Sb_2Te_3 crystal decreases the hole mobility, presumably by increased magnetic scattering which decreases the conductivity (Figures 1.3).

1.3 Theme and plan of the thesis

The aim of this work is to study the temperature dependence of the far-infrared optical properties of Sb_2Te_3, $Sb_{1.97}V_{0.03}Te_3$ and $Sb_{1.94}Cr_{0.06}Te_3$ using reflectance spectroscopy in the far infrared spectral range. The complex dielectric function (the quantity that houses information regarding the electronic as well as phonon properties of materials) can be obtained in this spectroscopy. This thesis will be presented in five Chapters. In Chapter 2, the theory of the optical properties of solids will be discussed. The chapter talks about the interaction of electromagnetic radiation with matter using Drude and Lorentz models as well as the dielectric constant, refractive index, Kramers-Kronig relations and sum rule. The materials background of Sb_2Te_3 and some related materials will be discussed in Chapter 3. Experimental methods employed in this work are discussed in Chapter 4 while Chapter 5 presents and discusses the experimental results. Finally, conclusions and suggestions for future work are presented in Chapter 6.

Chapter 2

Optical Properties Theory

2.1 Optical Properties of Solids

When light (electromagnetic radiation) is shone on a solid, the light can be absorbed, reflected or scattered, or transmitted by the solid. The interpretation of results obtained from the interaction of electromagnetic radiation with a solid is based on Maxwell's equations [7, 8, 9]. Optical spectroscopy (e.g. reflectance spectroscopy) experiments can be used to determine the complex dielectric function. The electronic structure of a material, excitations in the material and the mechanisms (i.e magnetism, superconductivity) that drive these excitations affect the complex dielectric function.

2.2 Optical constants, dielectric function and optical conductivity

Optical constants (e.g. real refractive index n and extinction coefficient κ) are used to characterize the propagation of electromagnetic radiation with wave vector k [7]. The electric field in a material varies from one point to the other due to the periodicity of the atomic lattice. The optical constants contain the response of a material to an applied electric field and are unique to a given material. The complex refractive index is given as

$$\tilde{N} = n + i\kappa \tag{2.1}$$

where n is the real refractive index and the imaginary part of the refractive index, κ is also known as the extinction coefficient. Suppose an electromagnetic wave is propagating in the z direction, then the electric field is given by

$$E = E_0 e^{i(kz-\omega t)} \tag{2.2}$$

where E_0 is the amplitude of the electric field, k is the wave vector of the electromagnetic radiation and ω is the angular frequency. Assuming the medium absorbs light

$$k = \tilde{N}\frac{\omega}{c} = (n+i\kappa)\frac{\omega}{c} \tag{2.3}$$

where c is the speed of light. Substituting equation (2.3) into equation (2.2), one obtains

$$E = E_0 e^{\left(\frac{-\kappa\omega z}{c}\right)} e^{i\left(\frac{\omega n z}{c}-\omega t\right)}. \tag{2.4}$$

The first exponential (real) in equation (2.4) describes the fact that electromagnetic wave is attenuated as it passes through the material. Other representations of the optical response include the complex dielectric function $\tilde{\varepsilon}$ and complex optical conductivity $\tilde{\sigma}$. The relation between the complex refractive index $(\tilde{N})$ and the dielectric function $\tilde{\varepsilon}$ is given as [7, 9]

$$\tilde{N} = \sqrt{\tilde{\varepsilon}}. \tag{2.5}$$

The dielectric function has a real part and an imaginary part combined as

$$\tilde{\varepsilon} = \varepsilon_1 + i\varepsilon_2. \tag{2.6}$$

Using Maxwell's equations, the complex conductivity $\tilde{\sigma}$ is related to $\tilde{\varepsilon}$ as follows:

$$\sigma_1 = \frac{\omega\varepsilon_2}{4\pi}, \tag{2.7}$$

$$\sigma_2 = \frac{\omega(\varepsilon_1 - 1)}{4\pi}. \tag{2.8}$$

The relation between ε_1, n, κ is given as

$$\varepsilon_1 = n^2 - \kappa^2 \tag{2.9}$$

and ε_2, n, κ are connected by the equation

$$\varepsilon_2 = 2n\kappa. \tag{2.10}$$

Solving equations (2.9) and (2.10), we obtain

$$n = \frac{1}{\sqrt{2}}\sqrt{\varepsilon_1 + \sqrt{\varepsilon_1^2 + \varepsilon_2^2}}, \tag{2.11}$$

$$\kappa = \frac{1}{\sqrt{2}}\sqrt{-\varepsilon_1 + \sqrt{\varepsilon_1^2 + \varepsilon_2^2}}. \tag{2.12}$$

Finally the near normal incidence reflectivity, which is what will be measured is given as

$$R = \frac{\kappa^2 + (n-1)^2}{\kappa^2 + (n+1)^2} \tag{2.13}$$

2.3 Kramers-Kronig Relations

A system responds in its own way when an external stimulus acts on it. The Kramers-Kronig relations give the relationship between the real and the imaginary parts of a complex response function. The complex response function could be written as

$$\tilde{G}(\omega) = G_1(\omega) + iG_2(\omega) \tag{2.14}$$

where $G_1(\omega)$ is the real part and $G_2(\omega)$ is the imaginary part of the function. $G_1(\omega)$ is an absorption process (i.e. involves a loss in energy of the electromagnetic waves), while $G_2(\omega)$ is a dispersive process (i.e involves a change in phase of the electromagnetic radiation). The

dispersion relations between the real part and the imaginary part of the response function
are:

$$G_1(\omega) = \frac{2}{\pi} P \int_0^\infty \frac{\tilde{\omega} G_2(\tilde{\omega})}{\tilde{\omega}^2 - \omega^2} d\tilde{\omega}, \tag{2.15}$$

$$G_2(\omega) = -\frac{2\omega}{\pi} P \int_0^\infty \frac{G_1(\tilde{\omega})}{\tilde{\omega}^2 - \omega^2} d\tilde{\omega}. \tag{2.16}$$

Equations (2.15) and (2.16) are known as Kramers-Kronig relations [7]. This dispersion
relation connects a dispersive process $G_2(\omega)$ to an absorption process $G_1(\omega)$ and vice versa.
The relation between the real and the imaginary parts of optical response functions and
optical parameters could be derived using these Kramers-Kronig's relations. Note that the
influence of $G_1(G_2)$ at a particular frequency ω affects the action of $G_2(G_1)$ throughout
the whole frequency range. Hence the Kramers-Kronig relation is said to be non-local in
frequency [7].

With reflectance spectroscopy, the real and imaginary parts of the response function can-
not be simultaneously determined. The analytical procedure for obtaining complex optical
constants from reflectance data is as follows: Reflectance R(ω) is the data obtained from the
laboratory experiments,

$$R(\omega) = |\frac{E_r}{E_i}|^2 \tag{2.17}$$

where E_i is the incident electric field and E_r is the reflected electric field which are related
by

$$E_r = r e^{i\theta(\omega_0)} E_i \tag{2.18}$$

where $\theta(\omega_0)$ is the phase angle and r $e^{i\theta(\omega_0)}$ is the complex reflectivity amplitude. The relation
between $\theta(\omega_0)$ and R(ω) is given by the Kramers Kronig relation [9]

$$\theta(\omega_0) = \frac{\omega_0}{\pi} \int_0^\infty \frac{ln[R(\omega)/R(\omega_0)]}{\omega_0^2 - \omega^2} d\omega. \tag{2.19}$$

Equation 2.19 can be solved with Simpson's rule [9]. In laboratory experiments, only the reflectance for a finite range of energies (frequencies) can be measured and a significant amount of the integral in equation 2.19 comes from frequencies that have not been measured. Hence extrapolations are made to experimental data in order to solve equation 2.19. An example is shown in Figure 2.1, for a material different from the ones studied in this work.
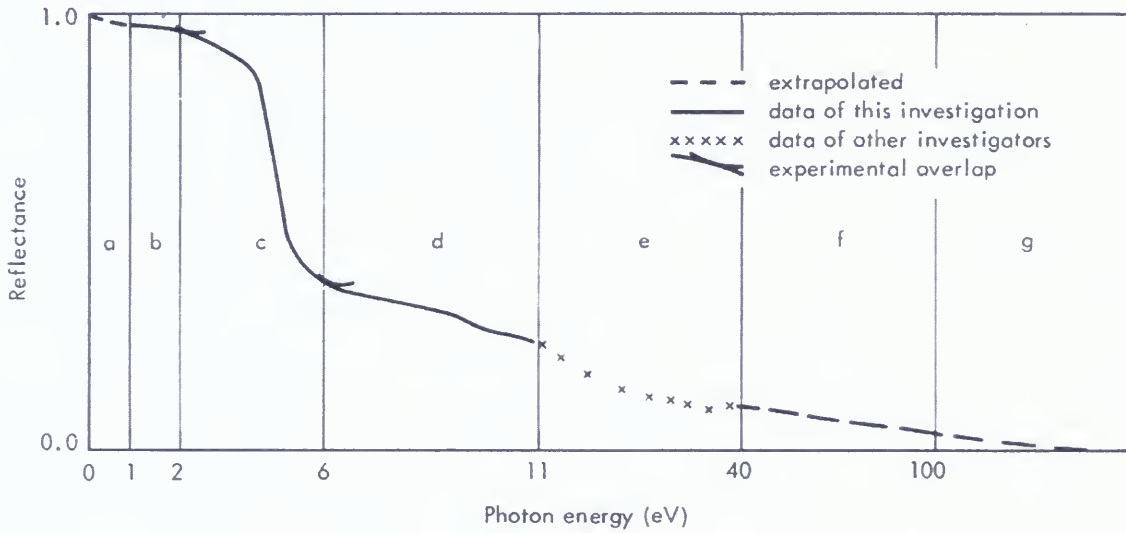
Figure 2.1: Reflectance Spectrum with regions: (a) low-energy extrapolation from photon energy close to zero to 1eV; (b) experimental data in the near infrared; (c) experimental data in the energy range 2-6eV; (d) spectrum in the energy range 6-11eV; (e) data from work performed from 11-40eV; (f) and (g) represent high energy extrapolation [9].

The refractive index n and extinction coefficient κ are given in terms of r(ω) and $\theta(\omega)$ as

$$n(\omega) = \frac{1 - r^2}{1 + r^2 - 2rcos\theta} \tag{2.20}$$

and

$$\kappa(\omega) = \frac{2rsin\theta}{1 + r^2 - 2rcos\theta} \tag{2.21}$$

respectively. The refractive index n and extinction coefficient κ given in equations 2.20 and 2.21 respectively could be substituted into equations 2.9 and 2.10 respectively, obtaining ε_1 and ε_2. The values of the dielectric function could be substituted into equations (2.7) and (2.8) obtaining conductivity. It should be noted that the process of obtaining the optical conductivity from experimental reflectance data is usually done with a computer program.

2.4 Qualitative discussion of Reflectance in Metals, Semiconductors and Insulators

To study the optical properties of a metal, the optical reflectance over a wide frequency range is needed. The reflectance of Au tends toward one at low frequencies (Figure 2.2)
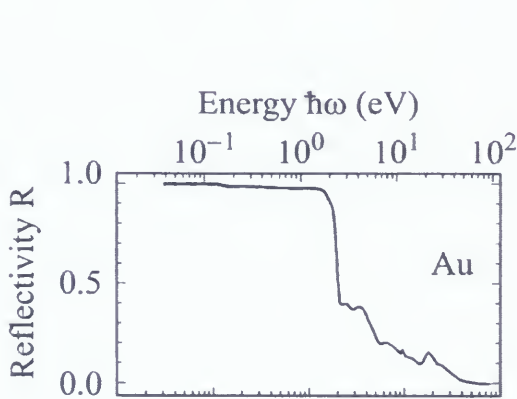
Figure 2.2: Reflectance spectrum of gold [7].
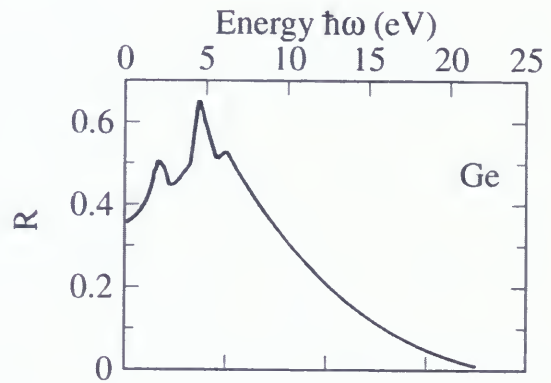
Figure 2.3: Reflectance spectrum of germanium [7].

and stays high until about 2eV called the plasma frequency which marks the beginning of the transparent regime (see Appendix A). In contrast to metals, the reflectance of a semiconductor or insulator (Figure 2.3) is not unity at low frequencies. The presence of free electrons causes the reflectance to tend to unity at low frequencies. Also, note that a combination of Drude and several Lorentz oscillators (see Appendix A) are necessary to account for the experimental reflectance of real materials. Hence the dielectric function could be written in such a model as
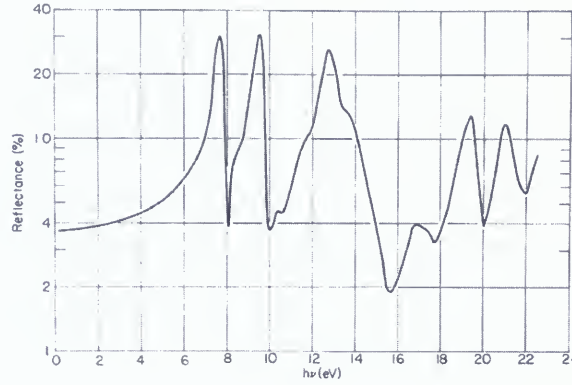
Figure 2.4: Reflectance spectrum of potassium chloride (kcl) [9].

$$\varepsilon(\omega) = \varepsilon_\infty - \frac{\omega_p^2}{\omega(\omega + i\Gamma)} + \Sigma_j \frac{\omega_{pj}^2}{\omega_{0j}^2 - \omega^2 - i\omega\Gamma_j} \qquad (2.22)$$

where ε_∞ is the contribution of the oscillators not included in sum where $\omega_{0j} \gg \omega$. The second term is a contribution from Drude (free electron term) while the third term is a summation of various Lorentz oscillators. Close to zero frequency, the reflectivity of Ge is around 0.35 (Figure 2.3) and increases with increasing frequency, forming two peaks before reaching the energy of about 5eV beyond which it then begins to decrease. The peaks in the reflectance spectrum of germanium (Figure 2.3) are due to interband transitions. In ionic or partially ionic materials, there will be more peaks at much lower energies or frequencies (i.e $100 - 1000\text{cm}^{-1}$) due to excitation of infrared active phonons. The single particle energy gap ϵ_g (0.70eV) of germanium obtained from direct current conductivity corresponds to a very weak Lorentz oscillator and is hard to see in Figure 2.3 since it is an indirect transition. The relation that connects the direct current conductivity and the energy gap is given as

$$\sigma_{dc}(T) = \sigma_0 e^{\frac{-\varepsilon_g}{2k_B T}} \qquad (2.23)$$

where the pre-factor σ_0 contains the number of carriers and their mobilities, k_B is Boltmann's constant and T is temperature. The energy gap ε_g is the energy required to thermally excite

an electron into the conduction band, leaving a hole in the valence band.

The difference between semiconductors and insulators is that the band gap of insulators is much larger than that of semiconductors. It should be noted that at very high frequencies ($\nu \to \infty$), the reflectivity R approaches zero (Figures 2.2 and 2.3), while for very low frequencies ($\nu \to 0$), R for metals (Figure 2.2) approaches one. Thermal excitation of charge carriers in semiconductors promote electrons from the valence band into the conduction band leaving behind a hole in the valence band, while the probability of thermal excitation occuring in an insulator is remote due to the large band gap (i.e. ε_g=7.5eV for Potassium Chloride, KCl) which the energy of the incident light should overcome for excitation to occur. In the reflectance spectrum of KCl (Figure 2.4), the first peak occurs near the energy gap.

Metals exhibit both intraband and interband transitions (Figure 2.5). An intraband transition is the excitation of an electron from a state below the Fermi level to a state above the Fermi level but within the same band and corresponds to the Drude term in equation 2.22. An interband transition is the excitation of an electron from a state below the Fermi level to a state in another band above the Fermi level corresponding to one of the finite frequency oscillators in equation 2.22.
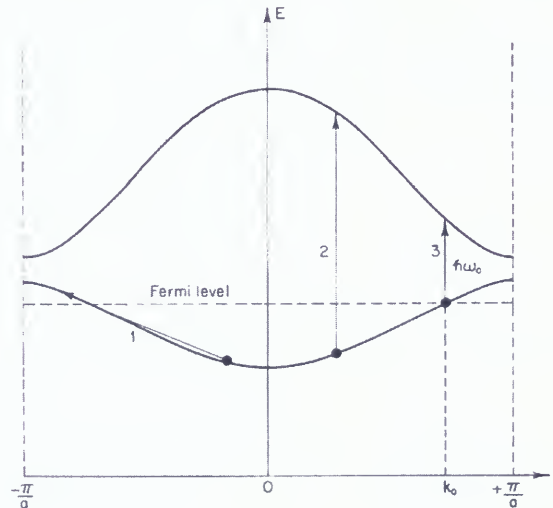
Figure 2.5: Schematic diagram showing intraband transition(1) and interband transition (2,3) [9]

The Drude model (Appendix A.2) can be used for intraband transitions, while the Lorentz model (Appendix A.1) is used for interband transitions or infrared active phonons. Intraband transitions have no thresholds (unlike interband transitions). The dielectric function can be decomposed into a contribution by intraband (Drude) transitions and that by interband or infrared active phonon (Lorentz) transitions [7]. It should be noted that when determining the optical properties of a metal over a wide frequency range, interband transitions should also be included (in addition to intraband transitions) to account for optical transitions between different bands in the metal. Hence an experimentally determined optical parameter ε_1^{exp} could be split into intraband and interband contributions as follows

$$\varepsilon_1^{exp} = \varepsilon_1^{intra}(\omega) + \varepsilon_1^{inter}(\omega). \tag{2.24}$$

At low frequencies ($\nu \to 0$), ε_1^{inter} is finite (Figure 2.6). The peak below $2 \times 10^4 \text{cm}^{-1}$ represents the onset of absorption [7]. Equations 2.22 and 2.24 are closely related, equation 2.24 could be viewed as coming out of equation 2.22.
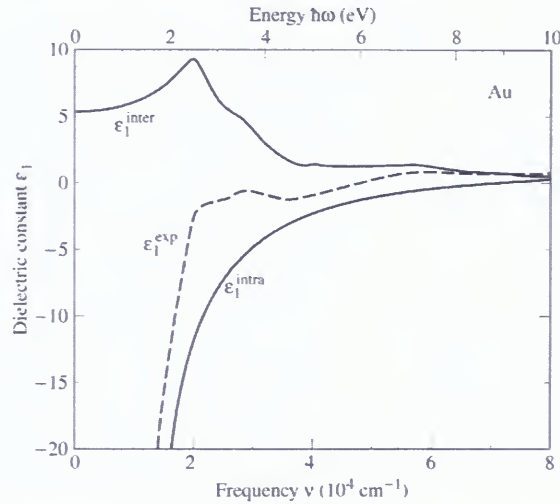
Figure 2.6: Dielectric constant of gold obtained from experiment ε_1^{exp} and its component parts ε_1^{inter} and ε_1^{intra} versus frequency. At low frequencies, ε_1^{inter} is finite and the peak in ε_1^{inter} represents the onset of absorption. [7].

Chapter 3

Materials Background

3.1 Bi_2Te_3 and Bi_2Se_3

Before discussing Sb_2Te_3, it is important to first take a look at some materials related to Sb_2Te_3 (i.e Bi_2Te_3 and Bi_2Se_3). Previous work on the optical properties of these materials will help us construct extrapolations for Kramers Kronig analysis as discussed in chapter 2. Bi_2Te_3 and Bi_2Se_3 are like Sb_2Te_3 in several ways: They are layered materials and have the same crystal structure. They are all susceptible to anti-site defects with excess Sb in Sb_2Te_3 and excess Bi in Bi_2Te_3 and Bi_2Se_3. They are narrow band semiconductors(i.e E_g=0.67eV, 0.15eV and 0.26eV for Bi_2Se_3, Bi_2Te_3 and Sb_2Te_3 respectively) [3, 4, 12]. Optical investigation of Bi_2Se_3 in the far infrared (Figure 3.1) reveals a gradual decrease of reflectance (R) with wave number ($\bar{v}$) from $\bar{v}$ close to zero to about 50cm^{-1} due to free carriers. The increase of R from about 50cm^{-1} to 75cm^{-1} shows the influence of a phonon. There is a gradual decrease of reflectance from 75 cm^{-1} to about 147 cm^{-1}, followed by a steep decrease from 147 cm^{-1} to 170 cm^{-1}. A minimum occurs at about 180 cm^{-1}, then a gradual increase until beyond 250 cm^{-1}. Köhler [10] suggested that the minimum would shift with a change in carrier concentration. This shift was observed by Thomas et.al. [13] and will be discussed below.

Reflectance measurements for Bi_2Te_3 and Bi_2Se_3 at 15K (Figures 3.2 and 3.3) [11] show almost the same features observed for Bi_2Se_3 at 300K the difference being that the features occured at different wave numbers and additional peaks were observed in Bi_2Te_3 (onset 116cm^{-1}) and Bi_2Se_3 (onset 120 cm^{-1}). The infrared active frequencies and oscillator pa-
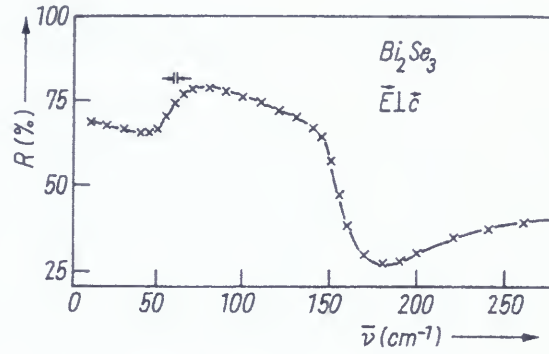
Figure 3.1: Far infrared reflectance as a function of wave number ($\bar{v}$) of Bi$_2$Se$_3$ at 300K. The electric field is perpendicular to c axis (E $\perp$ c)[10]
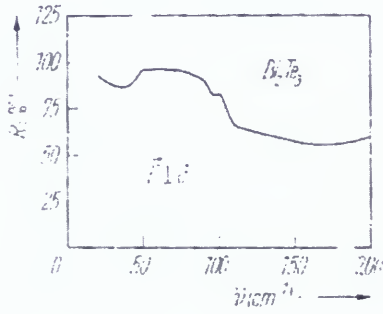
Figure 3.2: Far infrared reflectance variation of Bi$_2$Te$_3$ as a function of wave number at 15K with the electric field $\bar{F}$ perpendicular to c axis [11].
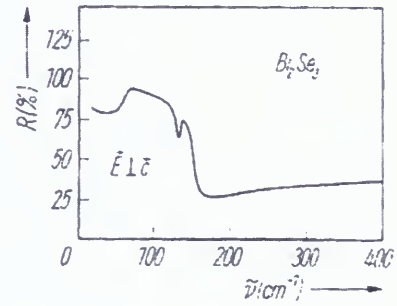
Figure 3.3: Far infrared reflectivity dependence of Bi$_2$Se$_3$ as a function of wave number at 15K with the electric field perpendicular to the c axis [11].

rameters derived from a classical fit (using equation 2.22) of reflectance data of Bi$_2$Te$_3$, Bi$_2$Se$_3$ at temperatures of 15K and 300K, and Sb$_2$Te$_3$ at a temperature of 300K are shown in Table 3.1. It could be observed that Γ_1 and ω_{p1} decrease as the temperature goes from 300K to 15K in Bi$_2$Te$_3$ and Bi$_2$Se$_3$. This is known as phonon softening. This softening was observed in our samples and will be discussed again in Chapter 5.

In optical studies of Bi$_2$Te$_3$ and Bi$_2$Se$_3$ from the far infrared to the far ultraviolet region of the electromagnetic spectrum, Greenaway and Harbeke [12] observed that if the electric field is perpendicular to the c axis (E$\perp$c), a peak appears around the energy corresponding

Table 3.1: Infrared active frequencies and oscillator parameters derived from a classical fit of Bi_2Te_3, Bi_2Se_3 at 300K and 15K; Sb_2Te_3 at 300K. [10, 11, 12]

	Bi_2Te_3		Bi_2Se_3		Sb_2Te_3
	300K	15K	300K	15K	300K
ε_∞	85	85	29	29	51
$\omega_1(cm^{-1})$	50±2	48±2	65±2	61±2	67
$\Gamma_1(cm^{-1})$	10	4	12	10	10
$\omega_{p1}(cm^{-1})$	716	687	592	556	1498
$\omega_2(cm^{-1})$	95±5	98±3	129±5	134±5	-
$\Gamma_2(cm^{-1})$	15	7	15	8	-
$\omega_{p2}(cm^{-1})$	116	120	91.2	94.7	-

to 6eV ($\approx$ 50,000cm^{-1}) for Bi_2Te_3 and 7eV for Bi_2Se_3. Thomas et. al. [13] measured the temperature dependent reflectance of a sample of Bi_2Te_3 with high concentration of anti-site defects, resulting in more free holes than the sample of Figure 3.2. Note that the plasma edge [Figure 3.4] occurs at higher photon energies as T decreases. This suggests that the plasma frequency and hence carrier density should increase as temperature decreases. This is quite unusual as the carrier density in semiconductors usually decreases with decrease in temperature due to carrier freezeout. Although Thomas et al. assumed a T independent scattering rate, the reflectance data (Figure 3.4) shows that the assumption of a constant Γ is not correct as the minimum of the reflectance spectrum gets deeper with decrease in temperature. Figures 3.5-3.7 illustrate how the reflectance spectrum for the Drude model (Appendix A.2) changes as a result of variation of gamma(Γ), epsilon infinity(ε_∞) and plasma frequency (ω_p). Note the effect of increased ω_p is to shift the plasma edge toward higher frequencies, the effect of gamma is to make the plasma edge more or less step like and the minimum deeper or shallower. A comparison of Figure 3.7 with Figure 3.4 suggests that Γ is decreasing with decreasing T. In Figure 3.6, one could observe that as ε_∞ is increased (with
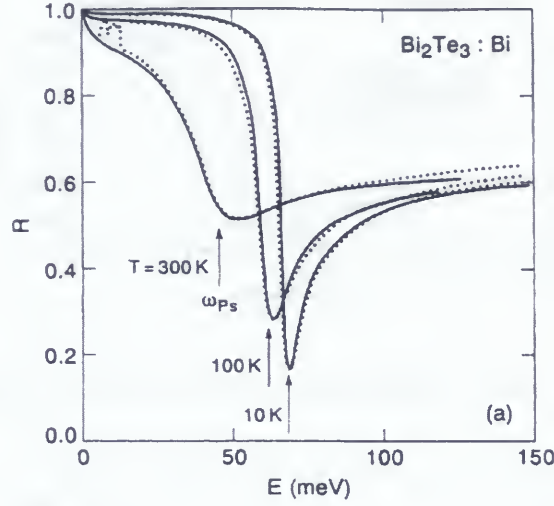
Figure 3.4: Far infrared(FIR) variation of reflectance as functions of energy and temperature. The minimum deepens with decreasing temperature [13]

ω_p and Γ held constant), the reflectance minimum becomes shallower and moves to smaller wave number.

3.2 Previous optical studies on Sb$_2$Te$_3$ and Sb$_2$Te$_3$ based materials

Lostak et. al. (Figure 3.8) [6] observed that adding chromium (Cr) atoms to Sb$_2$Te$_3$ crystal does not appreciably change the position of the plasma edge (dip near 1100cm^{-1}). Dyck et. al's investigation of the Hall effect and resistivity [4] suggests that the scattering rate of the carriers increase with Cr concentration because the Hall coefficient R$_H$, and therefore the carrier density does not change much. This will be discussed in detail in chapter 5. In Figure 1.3a, variation of Hall coefficient as a function of temperature for Sb$_{2-x}$Cr$_x$Te$_3$ was plotted. The relation between Hall coefficient (R$_H$) and carrier concentration is given as

$$R_H = \frac{-1}{ne} \tag{3.1}$$
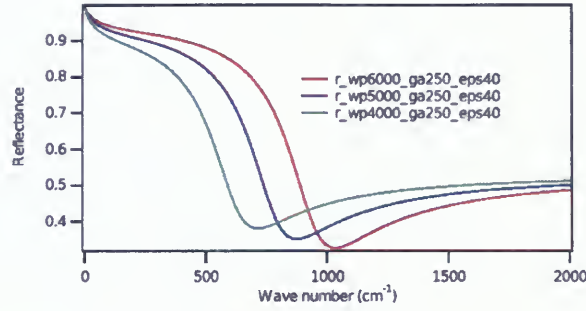
Figure 3.5: Nature of reflectance spectrum for variable ω_p= 6000,5000,4000cm^{-1}, fixed Γ=250cm^{-1} and ε_∞=40cm^{-1} .
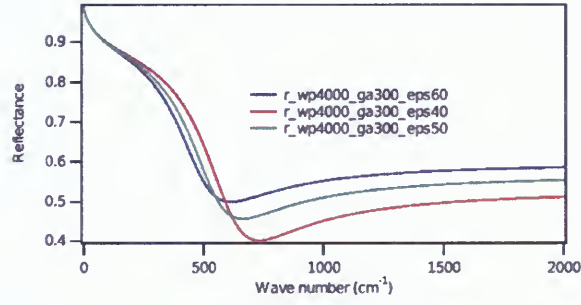
Figure 3.6: Change in reflectance spectrum for fixed ω_p=4000cm^{-1} and Γ=300cm^{-1}, but variable ε_∞= 60,40,50cm^{-1}.

where n is carrier concentration and e is elementary charge (e=1.6x10^{-19}C). The minimum value of R$_H$ for the curves in Figure 1.3a [4] is about 0.04cm^3/C, while the maximum value (for the curves) is a little less than 0.1cm^3/C. Using the above equation, one obtains a carrier concentration of between 6.25x10^{19}cm^{-3} and 1.56x10^{20}cm^{-3} for Cr concentration $0 \leq x \leq 0.095$.
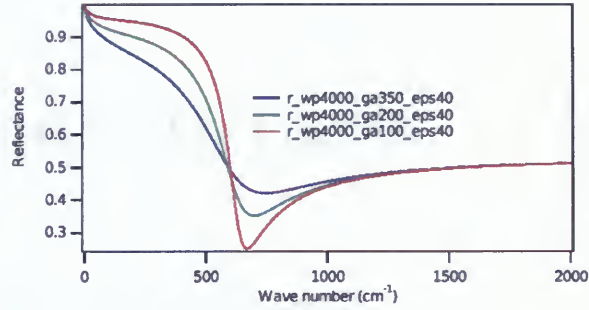
Figure 3.7: Variation of reflectance spectrum for fixed $\omega_p = 4000 \mathrm{cm}^{-1}$ and $\varepsilon_\infty = 40$ but variable $\Gamma = 350, 200, 100 \mathrm{cm}^{-1}$.
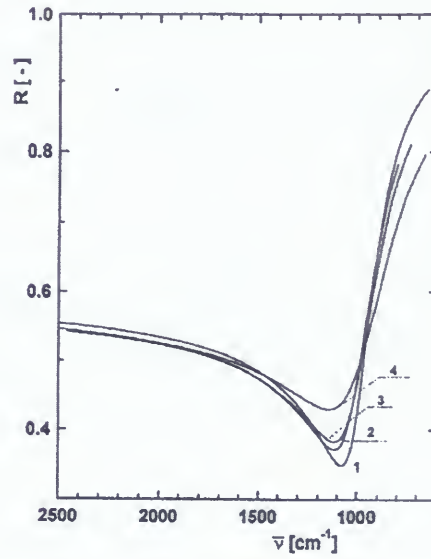
Figure 3.8: Reflectivity spectra of $Sb_{2-x}Cr_xTe_3$. The labelling corresponds to different concentrations of Cr, 1 corresponds to x=0, 2 corresponds to x=0.01, 3 corresponds to x=0.035 and 4 corresponds to x=0.07 [6]

Chapter 4

Experimental Methods

4.1 Resistivity Measurement

In this work, the resistivities of the samples were measured over the temperature range 5K-290K using the Van der Pauw technique [14]. In this technique, four contacts are made at the corners of a thin sample (Figure 4.1).
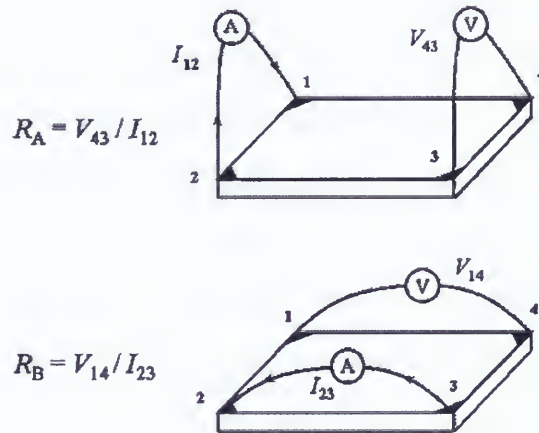
Figure 4.1: Schematic diagram of the Van der Pauw technique [14].

The sample should be free of holes. Current is passed through one edge of the sample and voltage is measured at the opposite edge. Then the probes are removed and connected to the adjacent sides and the same procedure is repeated. Resistances R_A and R_B are determined as shown in Figure 4.1. Van der Pauw showed [14] that the sample resistivity ρ is related to

R_A and R_B through the equation;

$$exp(\frac{-\pi R_A t}{\rho}) + exp(\frac{-\pi R_B t}{\rho}) = 1 \qquad (4.1)$$

where t is the thickness of the sample. It should be noted that the Van der Pauw technique should be used for only thin samples with negligible thickness compared to the length and width of the sample.

In this experiment, four small (3 x 1.5mm and thickness 0.28mm) copper squares were glued on the corners of a mica slide (2 x 0.85cm and thickness 0.2mm) with Epoxy 907 adhesive system. Copper wires were soldered to the surfaces of the copper slides using indium. The samples, $Sb_{1.97}V_{0.03}Te_3$ (5mm x 5mm and thickness, 1.03mm), $Sb_{1.94}Cr_{0.06}Te_3$ (5mm x 5mm and thickness, 2.46mm), and Sb_2Te_3 (5mm x 5mm and thickness, 2.04mm) were mounted (i.e. one sample per experiment) to the centre of the mica slide with GE-varnish. Four tiny gold wires were attached with a very small amount of silver paint at the corners of the sample(s) while the other ends were each attached to the copper squares by pressing them into the indium and then applying a small amount of silver paint. This ensures contact of the gold wires with the copper wires, hence forming ohmic contacts.

The mica slide containing the sample was glued to a copper block at the end of a long (1.5m) stainless steel tube with copper wires running through it, making contact with the sample while the other end is connected to the computer controlled switches, current source and voltmeter. The stainless steel tube containing the sample was gradually lowered (one inch at a time with a waiting period of about 10 minutes between push-downs) to a 100 litre dewar of liquid helium. It should be noted that the dewar was less than a quarter full. The temperature changed from about 290K (corresponding to the first push down) to 5K (corresponding to the moment the rod was touching the liquid helium). The computer recorded the values of the Van der Pauw parameters for each temperature attained.

4.2   Reflectance Spectroscopy

It was mentioned in section 2.1 that optical spectroscopy experiments can be used to determine the complex dielectric function. Also mentioned was the fact that the electronic structure of a material, excitations in the material and mechanisms that drive these excitations can be obtained from the complex dielectric function. Reflectance spectroscopy near normal incidence is the type of optical spectroscopy used in this work. The reflectance of a sample is the ratio of the reflected intensity of the electromagnetic radiation from the sample to that of the incident intensity on the sample. The experimental apparatus include a light source spectrometer (a Michelson Interferometer), sample cryostat and detector.

Two types of systems were used in this work:

Michelson interferometer (Bruker IFS) or Fourier transform infrared (FTIR) spectrometer coupled to the Janis cryostat(for 45K $\leq$ T $\leq$ 300K).

Michelson interferometer (Bruker IFS) coupled to He^3 cryostat (for 0.3K $\leq$ T $\leq$ 50K). The experimental apparatus that is discussed in this thesis is that of the first in the list. The Bruker IFS coupled to He^3 cryostat is discussed in the M.Sc. thesis of Ocadlik [15].

4.2.1   Light Source

The light source used in this work was a Michelson Interferometer housed in a Bruker IFS 66v/S spectrometer. In a Michelson Interferometer, the beam splitter divides the electromagnetic radiation from the source into two parts, one part goes towards a movable mirror while the other part moves towards a fixed mirror. Some michelson interferometers have compensators to ensure that the paths of the light from the beam splitter to the movable mirror and the fixed mirror are identical. The two beams form interference patterns on the detector after being reflected by the mirrors and recombined by the beam splitter. The Bruker was kept under a vacuum of about 3mbar throughout the experiment. In this work, several optical components (Table 4.1) were used depending on the frequency range of interest.

Table 4.1: Types and working frequency ranges of components used in this work

Component	Type	Working frequency range (cm^{-1})
Detector	Bolometer(4.2K)	50-700
	MCT	450-5000
BeamSplitter	$50\mu m$ Mylar	10-55
	$6\mu m$ Mylar with Ge	60-650
	Ge on KBr	370-7500
Light Source	Globar(MIR)	30-7500
Window	Polypropylene	10-700
	KRS-5	300-7000

4.2.2 Sample Chamber

There was an optical table in the Bruker that contains a collection of plane and toroidal mirrors Figure 4.2 [16]. This optical table directs the light path from the spectrometer to the sample cryostat to the detector through a series of reflections. The sample chamber is separated from the light source by a window and was completely redesigned for this thesis. The window could (depending on the light source and detector) be any of those mentioned in Table 4.1. The sample was glued on the tip of a brass cone as shown in Figure 4.3, which was screwed on to the copper block. This allows for easy temperature variation of the sample. Previous students (Klassen, Liu) [16, 17] used a system where the sample was attached directly to the cold finger of the Janis cryostat and the light could be made to follow either the sample path or the reference path by moving the flip mirror shown in Figure 4.2.

In the redesigned system the reference path of Figure 4.2 was not used. Instead, a stepping motor which causes the sample holder to rotate between sample and reference on a vertical axis was mounted (Figure 4.4) while the Janis cryostat is mounted so that the liquid helium transfer tube enters the cryostat horizontally and brings down the temperature from
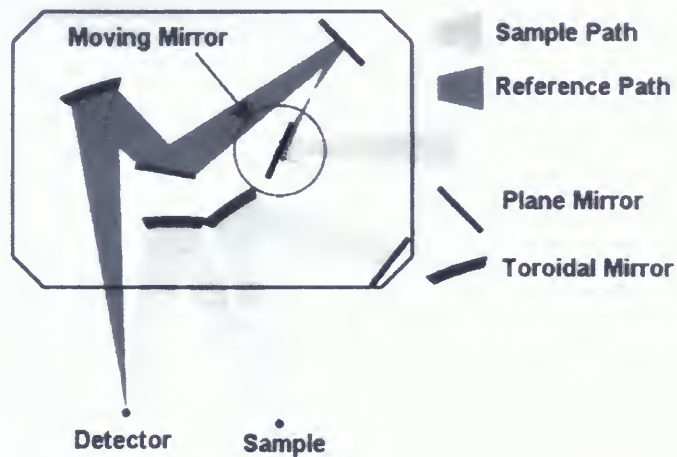
Figure 4.2: Optical table in the Bruker [16]

Figure 4.3: The sample $Sb_{1.97}V_{0.03}Te_3$ glued on the tip of a brass cone. $Sb_{1.94}Cr_{0.06}Te_3$ and Sb_2Te_3 look similar to the shown picture.

room temperature to about 38K (Figures 4.5). The L bracket where the sample and reference mirror are mounted in the new system is shown in Figure 4.6.
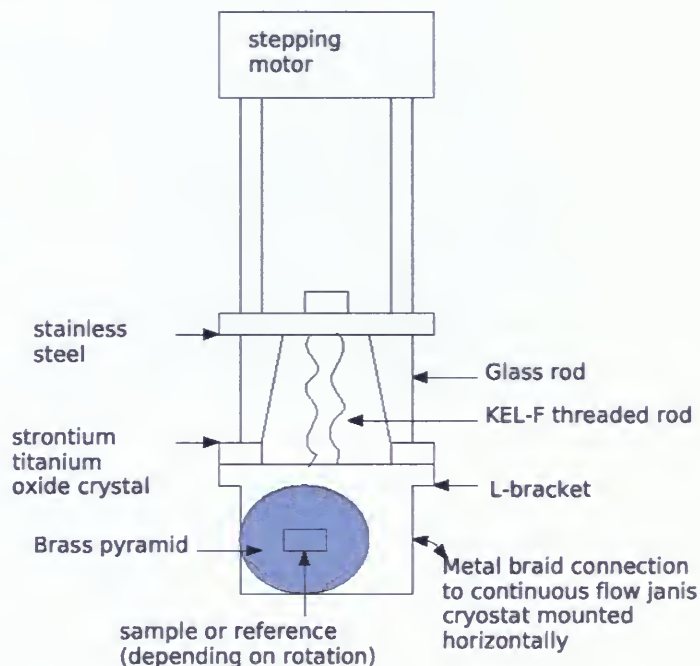
Figure 4.4: Components of the new system.

The temperature of the sample cryostat was varied (controlled) by a combination of varying helium flow rate and resistive heating controlled by a CRYO.CON.32 temperature regulator. The sample chamber was evacuated to a pressure of about 3×10^{-7} mtorr using roughing and turbo pumps in order to cool the sample and to allow a good quality in-situ gold evaporation. The reason for the redesigned sample chamber was that with the old system where the sample was mounted directly on the cold finger, the sample position moved significantly as the system was cooled from room temperature to 4K. The sample signal changed by over a factor of 2 with the greatest change occuring between 295K and 100K.

It was suspected that the sample did not go back to exactly the same position during the second temperature cycle after gold evaporation. Hence a new system was designed in
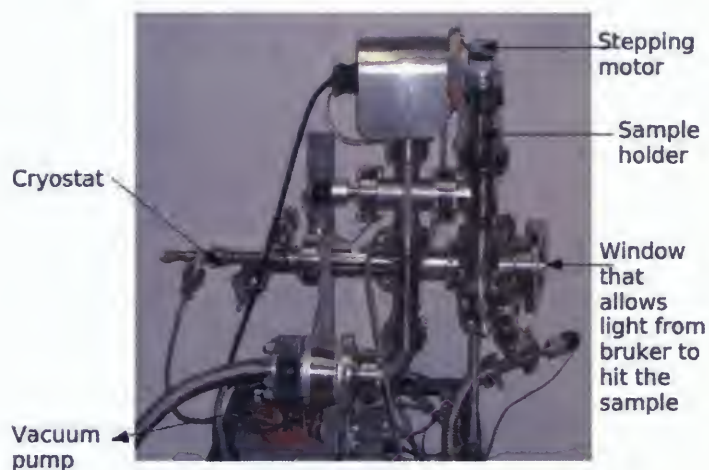
Figure 4.5: The new system showing the cryostat, vacuum pump, sample holder and window that allows light from the bruker to hit the sample.

Figure 4.6: Part of the sample holder showing reference mirror glued on brass cone and mounted on copper block. The sample is mounted on a pyramid (shown in Figure 4.3) and screwed on the other side of the L bracket (where the other three screws are).
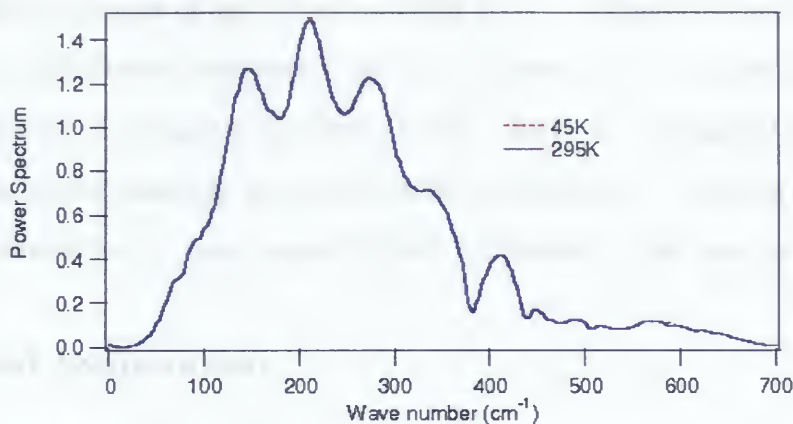
Figure 4.7: Power spectra of the reference at 45K and 295K. The fact that the spectra are the same signifies that the sample and reference mirror did not significantly shift throughout the duration of the experiment.

which the sample and reference were mounted on adjacent sides of a copper block (Figure 4.6) and the sample holder was connected to the cold finger using four copper braids. The power spectrum of reference is shown for the temperatures 45K and 295K (Figure 4.7). The fact that the spectra are almost at the same level shows that the sample and reference didn't significantly shift throughout the duration of the experiment. In our experiment a radiation shield was not used because some adjustments still need to be made to allow for free rotation of the sample holder. The lowest temperature achieved with the new sample holder was 38K. Hopefully, this can be improved after adjustments are made permitting the use of a radiation shield and better thermal contact (i.e more copper braids) connecting the sample to the cold finger.

4.2.3 Detectors

The detectors used in this work were a Bolometer and Mercury Cadmium Telluride (MCT). The bolometer was used to measure the reflectance of the sample over the wave number range of about $50cm^{-1}$ to $550 cm^{-1}$. The Bolometer operates on the principle that incoming electromagnetic radiation absorbed by the bolometer increases its temperature which induces

a change in the resistance of the bolometer. The MCT is a photoconductive detector used to measure the reflectance from about 450 cm^{-1} to 6000 cm^{-1}. It is an alloy of Mercury Telluride (HgTe) and Cadmium Telluride (CdTe). HgTe is a semimetal while CdTe is a semiconductor with a band gap of around 1.6eV (≈ 13000cm^{-1}). Alloying HgTe and CdTe produces a material with a band gap of 0.056eV (≈ 450cm^{-1}) (the band gap of MCT).

4.2.4 Gold Evaporation

Gold evaporation is carried out in order to obtain the absolute reflectance. Some of the light that falls on the surface of the sample could be scattered due to the nature of the surface of the sample. Hence the sample surface is coated with a thin layer of gold, since gold has a high, approximately constant reflectivity in the infra-red spectrum range. It should be noted that only the sample is coated with gold during the evaporation as the reference does not face the evaporation coils. To determine the reflectance of a given sample, one obtains the ratio of the intensity of light reflected by the sample I_a to that reflected by the reference mirror I_b. Then one evaporates gold(Au) on the sample and obtains the ratio of the intensity of light reflected by the sample I_c to that reflected by the reference I_d. The absolute reflectance is given as:

$$R_{abs} = \frac{\frac{I_a}{I_b}}{\frac{I_c}{I_d}} \tag{4.2}$$

The intensity ratios and absolute reflectance of Sb$_{1.97}$V$_{0.03}$Te$_3$ at 295K obtained using equation 4.2 are shown in Figure 4.8. Note that all the spurious structure in the spectra of Figure 4.7 (which is due to sample geometry) has cancelled out in the gold correction.
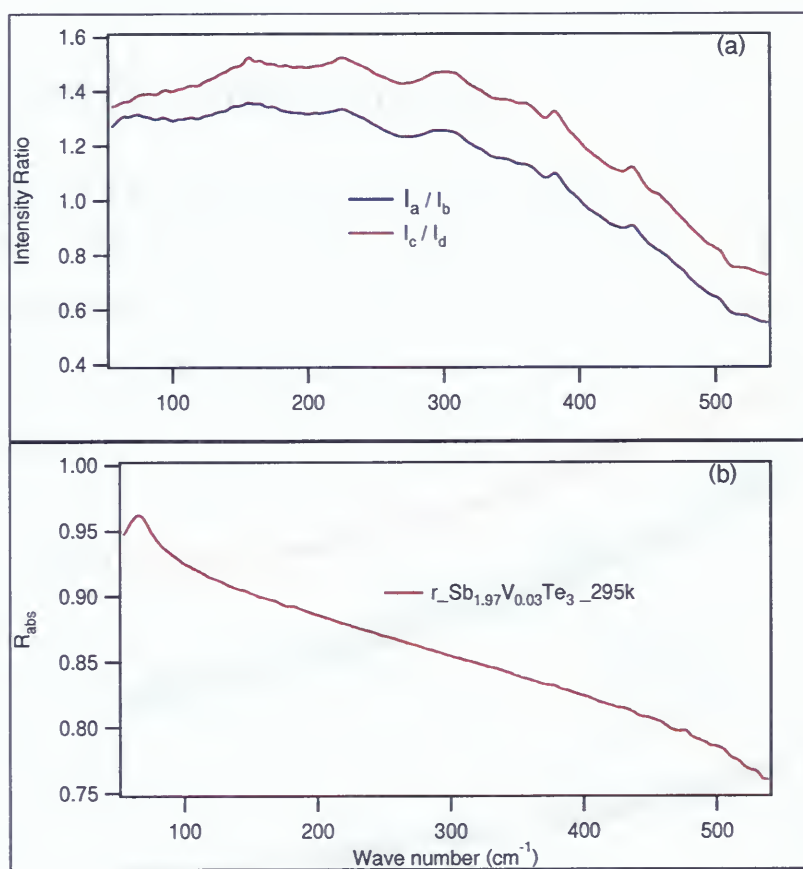
Figure 4.8: Intensity ratios (a) and R_{abs} (b) of $Sb_{1.97}V_{0.03}Te_3$ at 295K obtained using equation 4.2.

Chapter 5

Results and Discussions

5.1   Resistivity Measurements

Resistivity measurements were carried out on the samples Sb_2Te_3, $Sb_{1.97}V_{0.03}Te_3$ and $Sb_{1.94}Cr_{0.06}Te_3$ provided by Dr C. Uher and Dr P. Lošt'ák. The resistivities of the samples $Sb_{1.97}V_{0.03}Te_3$ and $Sb_{1.94}Cr_{0.06}Te_3$ were measured twice while that of Sb_2Te_3 was measured once .
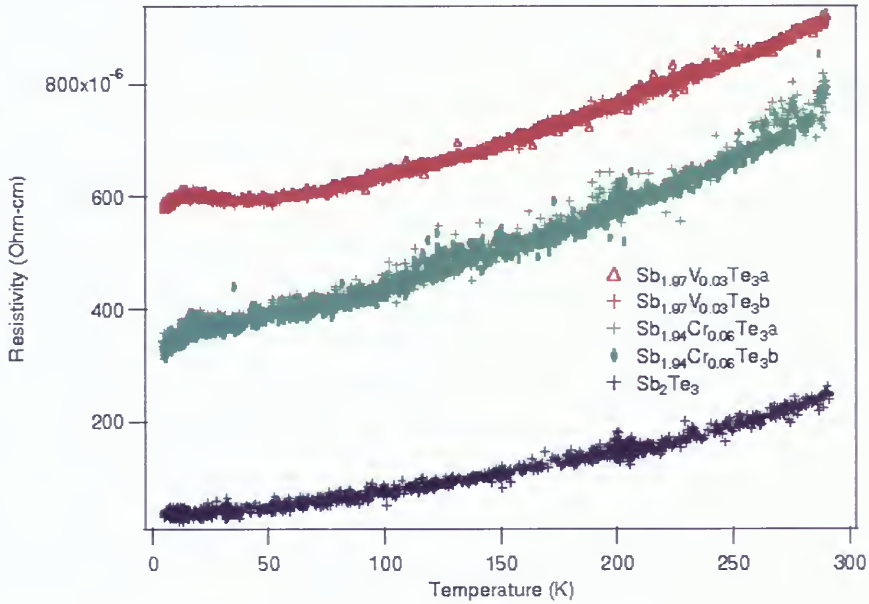
Figure 5.1: Resistivity versus Temperature graphs of $Sb_{1.97}V_{0.03}Te_3$, $Sb_{1.94}Cr_{0.06}Te_3$ and Sb_2Te_3. The numbering (a,b) represents the number of times the experiment was performed.

It can be observed (Figure 5.1) that for the undoped sample (Sb_2Te_3), resistivity increases with increase in temperature and there is no transition temperature unlike the doped samples. For the doped samples, the resistivity increases with temperature from about 5K to the Curie

temperature, T_C where a peak is formed. It then decreases, reaches a minimum, and then continues the increase with temperature. The T_C is between 16-22K for both doped samples.

If one compares the resistivity values obtained in this work with those obtained by Dyck et al., it can be observed that the data values obtained in this experiment for Sb_2Te_3 are close to that of Dyck et al. (Figures 1.4 and 1.3b), while those of $Sb_{1.97}V_{0.03}Te_3$ and $Sb_{1.94}Cr_{0.06}Te_3$ are not as close. It should be noted that before this resistivity experiment was performed, several optical reflectance experiments had been done with the samples being studied. The surfaces of the samples are usually coated with gold after each experiment. This gold is removed with transparent tape before the commencement of another experiment in other to get a clear clean surface of the sample. In the process, some layers of the sample are removed. The doped elements (i.e. V and Cr) are not evenly distributed across the sample layers. Perhaps that is why the values of the resistivities measured in this work differ from those of Dyck et. al. for $Sb_{1.97}V_{0.03}Te_3$ and $Sb_{1.94}Cr_{0.06}Te_3$.

5.2 Reflectance

The mid-infrared reflectance measurement of the samples used in this work is shown for the wave number range 500-7000cm^{-1} in Figure 5.2 [18]. It can be observed that the three reflectance curves in Figure 5.2 all have a minimum at about 1100 cm^{-1}. As shown in the appendix, the minimum occurs at ω_p and is given as (equation A.15)

$$\omega_p = \frac{4\pi p e^2}{m},\tag{5.1}$$

where N in equation A.15 is replaced with p here because holes are the majority carriers in our samples. Since the same location of the minimum means that the plasma frequencies (ω_p) are the same, one could say from the above equation that $\frac{p}{m}$ (ratio of carrier density to effective mass of the sample) does not change as well. Hence the result here agrees with Lostak et.al's observation that the carrier concentration of Sb_2Te_3 is not affected strongly by doping with
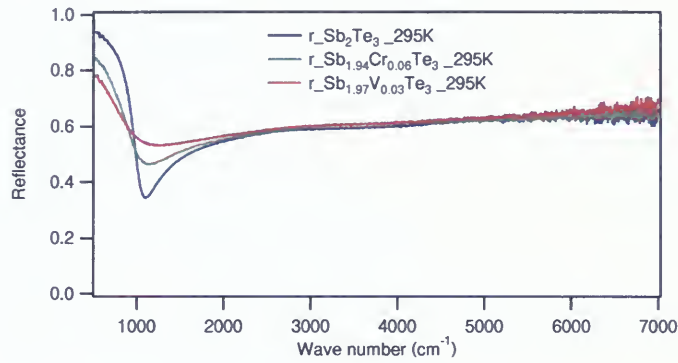
Figure 5.2: Reflectance of the samples $Sb_{1.97}V_{0.03}Te_3$, $Sb_{1.94}Cr_{0.06}Te_3$ and Sb_2Te_3 as a function of wave number (cm^{-1}) in the range 500-7000 cm^{-1}. The minimum of the graphs occur at almost the same frequency (≈ 1100 cm^{-1}), suggesting that there is no significant change in carrier concentration on doping Sb_2Te_3 [18].

V or Cr, highlighted in section 3.2. The reflectance data for Sb_2Te_3, $Sb_{1.94}Cr_{0.06}Te_3$ and $Sb_{1.97}V_{0.03}Te_3$ are shown in Figures 5.3-5.5. In addition an experiment was performed with the He^3 cryostat at 0.5K and 50K. This was done because we thought that perhaps something interesting might be observed in our sample at low temperature (e.g 0.5K). However, we did not observe any additional feature in the sample by using the He^3 cryostat (Figure 5.6). Hence, we did not do further measurements or analysis at 0.5K.
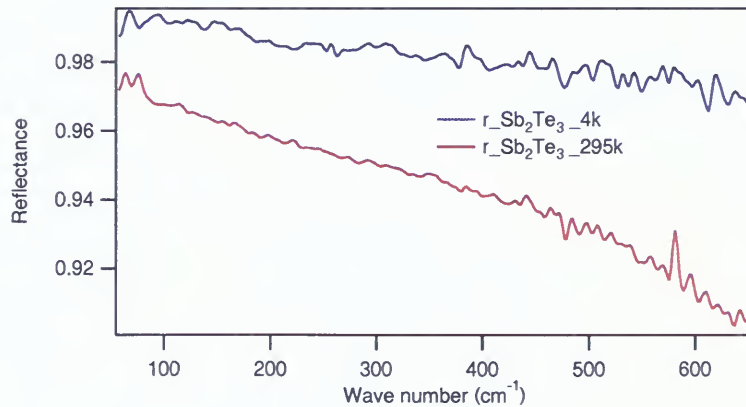
Figure 5.3: Far infrared reflectance data for Sb_2Te_3 at 295K and 4K.

It can be observed that on the average, reflectance decreased with increasing temperature
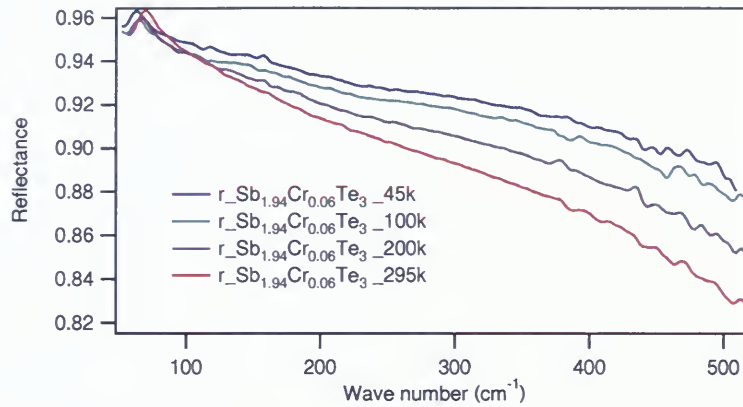
Figure 5.4: Reflectance spectra of $Sb_{1.94}Cr_{0.06}Te_3$ at 45K, 100K, 200K and 295K measured at the Far infrared (FIR) .

(Figures 5.3-5.6). Also reflectance R decreases as the wave number increases except in the case of the doped samples, where peaks indicating the presence of an infrared phonon mode are seen below $100cm^{-1}$. These peaks narrow and move slightly to lower wave number with decreasing temperature, a term referred to as phonon softening. This was also observed in isostructural Bi_2Se_3 and Bi_2Te_3 as discussed in section 3.1.
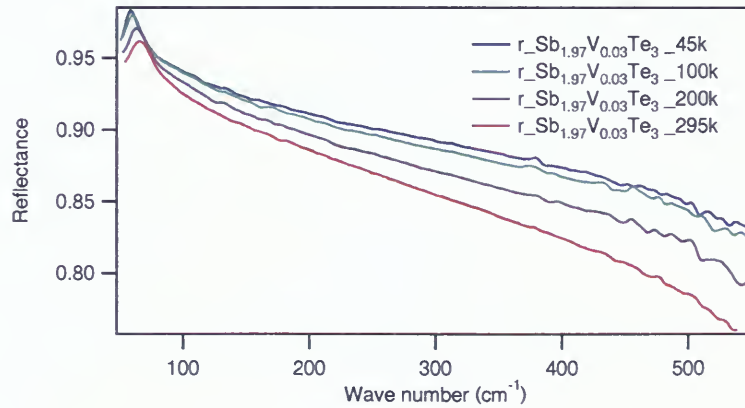
Figure 5.5: Far infrared reflectance spectra of $Sb_{1.97}V_{0.03}Te_3$ at 45K, 100K, 200K and 295K.
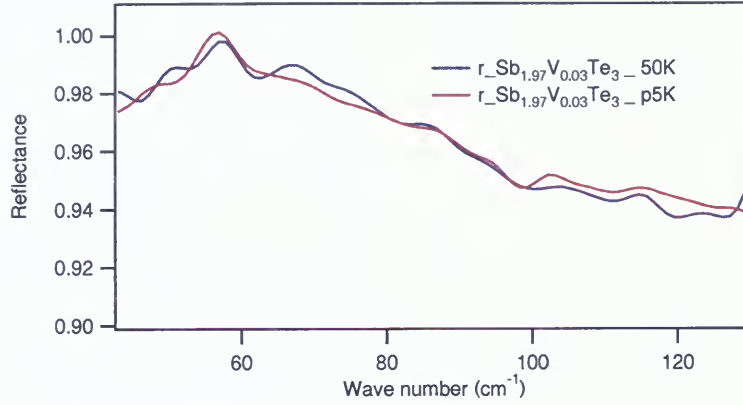
Figure 5.6: FIR Spectrum of the experiment on $Sb_{1.97}V_{0.03}Te_3$ performed with He^3 cryostat at 0.5K and 50K .

5.3   Extrapolations

The data available for KK analysis include FIR ($50cm^{-1}$- $550cm^{-1}$) at the temperatures of 45K, 100K, 200K and 295K as well as mid- infrared ($450cm^{-1}$ to $6500cm^{-1}$) at 295K. The frequency (wave number) regions covered in this experiment are $50-550cm^{-1}$ and $450-6500cm^{-1}$ (adding the data from my predecessor) [18]. In order to perform KK analysis, the data should be extrapolated to higher frequencies. The bolometer used in this experiment could detect radiation from about $50-600cm^{-1}$. Also the integral in section 2.3 begins from zero, so it is imperative to have data that is close to zero. Consequently, extrapolation had to be made from $1-55cm^{-1}$ for all the temperatures. The data were also extrapolated from $530cm^{-1}$ to $6000cm^{-1}$ for all temperatures except 295K. Finally, because a wide frequency range is needed to perform KK analysis, all data were extrapolated from $6000cm^{-1}$ to $200000cm^{-1}$.

5.3.1   High frequency extrapolations

A reflectance data set for Sb_2Te_3 at 295K was available from $50-15000cm^{-1}$. I measured from $50-550cm^{-1}$, while my predecessor [18] measured from $450-15000cm^{-1}$. Greenaway and Harbeke [12] measured the reflectance of Bi_2Te_3 from 0.1eV ($800cm^{-1}$) to 11eV ($88000cm^{-1}$)
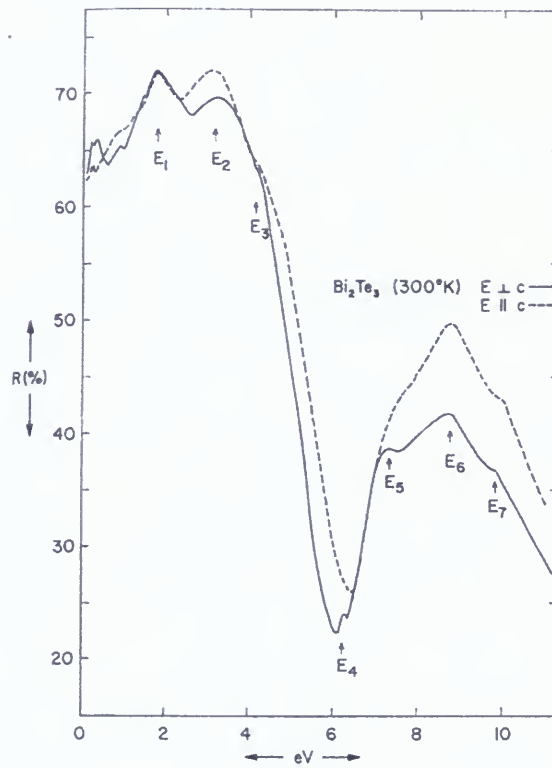
Figure 5.7: Reflectance spectra of Bi$_2$Te$_3$ at room temperature from far infrared to far ultraviolet with the electric field perpendicular (E⊥c) as well as parallel to c axis (E∥c) [12].
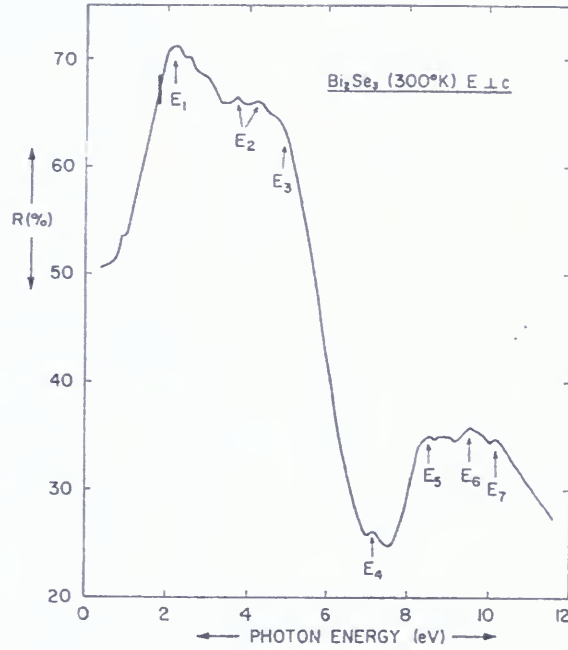
Figure 5.8: Reflectance spectrum of Bi_2Se_3 from 0.4eV to 11.5eV at 300k, with E⊥c [12].

and that of Bi_2Se_3 from 0.4eV ($3200cm^{-1}$) to 11.5eV ($92000cm^{-1}$) with the electric field perpendicular to c axis (E⊥c) in both cases. They observed that the spectra essentially have two main peaks (Figures 5.7 and 5.8) each with a triplet structure. A peak (E_4) was observed around 6eV($\approx 50000cm^{-1}$) [12] (Figure 5.7). For this work, I therefore also assumed the reflectance would have two large peaks. The reflectance data was fit between 50-$15000cm^{-1}$ for the sample Sb_2Te_3 assuming five oscillators and a Drude contribution (Drude ω_p=7574.23cm^{-1}, Γ_{Drude}=186cm^{-1}). A phonon was fixed at ω_0=67cm^{-1}, ω_p=1500cm^{-1}, Γ=10cm^{-1} since the studies by W. Richter et al. on V_2-VI_3 (i.e Sb_2Te_3) [11] as shown on Table 3.1 gave an idea of the values of these phonon parameters. We fixed ε_∞ to the value of one because of the high frequency oscillators. Also an oscillator was fixed at ω_0=50000cm^{-1} because of the observation by Greenaway and Harbeke [12] that there is an increase in reflectance at 6eV ($\approx 50000cm^{-1}$) as highlighted in the first paragraph of this section. An extrapolation from 1-200000cm^{-1} using the fit parameters of Table 5.1 is shown in Figure

5.9.
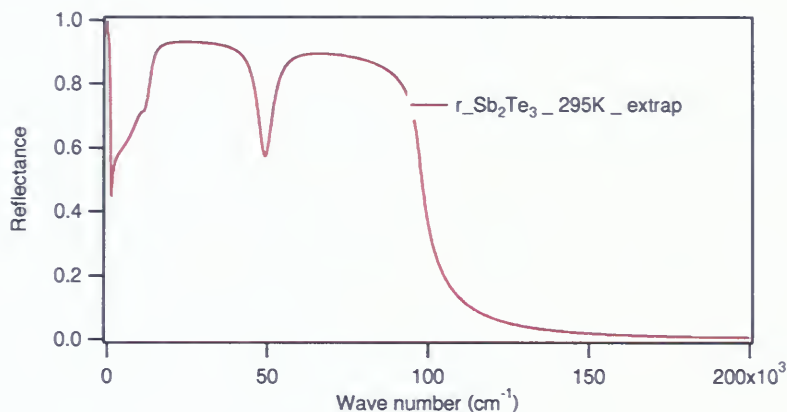
Figure 5.9: FIR reflectance spectrum of Sb_2Te_3 at 295K extrapolated from 1-200000cm^1. The curve fit parameters are shown in Table 5.1.

5.3.2 Low Frequency and Mid Infrared extrapolations

Since the available mid-infrared data from my predecessor is only for 295K, fits were performed on 4K, 45K, 100K and 200K FIR (50-550cm^{-1}) data using one Drude and five oscillators, but allowing only the Drude and phonon parameters free while fixing all other parameters. The fit parameters are listed in Table 5.2. Low frequency (1-55cm^{-1}) and mid infrared extrapolations (530-6000cm^{-1}) were made using the parameters of Table 5.2 plus the four high frequency oscillators of Table 5.1 which were assumed to be temperature independent. A sample graph showing what the extrapolations look like is displayed in Figure 5.10. It should be noted that there are seven such graphs, but just one is displayed since they are all similar. Low frequency (1-55cm^{-1}) and mid infrared extrapolations (530-6000cm^{-1}) were performed after fitting the data.

Table 5.1: High frequency extrapolation fitting parameters. The highest frequency oscillator centered at $\omega_0=50000$ was fixed. The parameters refer to Equation 2.22. They are all in cm^{-1} except for ε_∞ which is unitless.

	Value	Parameter
1	7574.23	Drude ω_p
2	185.699	Drude Γ
3	1	ε_∞
4	67	ω_{01}
5	10	Γ_1
6	1500	ω_{p1}
7	6609.48	ω_{02}
8	1767.59	Γ_2
9	11659.7	ω_{p2}
10	10731.1	ω_{03}
11	3774.32	Γ_3
12	48257	ω_{p3}
13	13702.2	ω_{04}
14	2224.46	Γ_4
15	77783.4	ω_{p4}
16	50000	ω_{05}
17	5000	Γ_5
18	20000	ω_{p5}

Table 5.2: Fitting parameters of the samples on which low and mid infrared extrapolations were performed.

Sample	$\omega_{pDrude}(\text{cm}^{-1})$	$\Gamma_{Drude}(\text{cm}^{-1})$	$\omega_0(\text{cm}^{-1})$	$\Gamma(cm^{-1})$	$\omega_p(\text{cm}^{-1})$	T(K)
Sb_2Te_3	7235 ± 87	52 ± 1	62 ± 0	10 ± 0	1500 ± 0	4
	7011 ± 56	167 ± 2	67 ± 0	10 ± 0	1500 ± 0	295
$Sb_{1.97}V_{0.03}Te_3$	7319 ± 37	440 ± 4	54 ± 0.2	4 ± 0.3	1506 ± 15	45
	7430 ± 48	470 ± 6	54 ± 0.2	5 ± 0.5	1457 ± 21	100
	8272 ± 107	658 ± 15	56 ± 0.2	9 ± 0.5	1450 ± 15	200
	6707 ± 22	572 ± 4	58 ± 0.2	11 ± 0.4	1267 ± 10	295
$Sb_{1.94}Cr_{0.06}Te_3$	7013 ± 33	262 ± 2	59 ± 0.4	9 ± 1.1	790 ± 36	45
	6947 ± 23	278 ± 2	61 ± 0.5	7 ± 1.3	570 ± 38	100
	6676 ± 22	325 ± 3	61 ± 0.7	19 ± 1.8	1250 ± 38	200
	6340 ± 16	376 ± 3	61 ± 0.5	21 ± 0.9	1706 ± 21	295
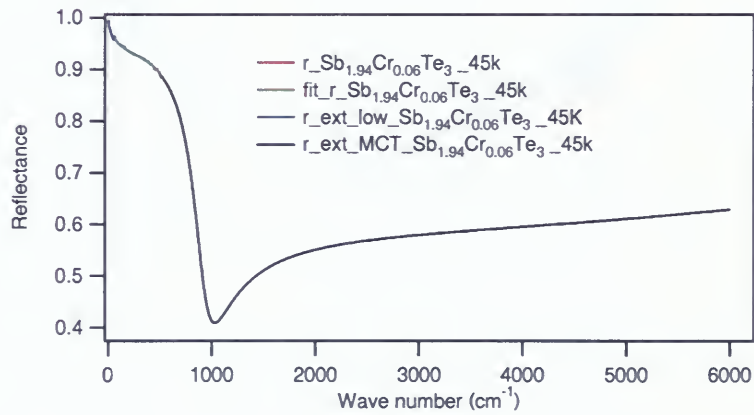
Figure 5.10: FIR reflectance and extrapolations from 1-55cm^{-1} and from 530-6000cm^{-1} of $Sb_{1.94}Cr_{0.06}Te_3$ at 45K. The Drude and phonon parameters used to make the extrapolations are listed in Table 5.2

5.4 Kramers Kronig (KK) Analysis and Optical conductivity

Some measurements were taken by my predecessor [18] at 295K for the samples Sb_2Te_3, $Sb_{1.94}Cr_{0.06}Te_3$ and $Sb_{1.97}V_{0.03}Te_3$ from $530cm^{-1}$ to $6000cm^{-1}$. Though my predecessor did some fits on the sets of data, he did not perform KK analysis that would yield the optical conductivity. Using the 295K FIR reflectance data of Figures 5.3 - 5.5, the mid infrared data of Figure 5.2 and the extrapolations discussed above, the KK derived optical conductivity was calculated and is shown in Figure 5.11. It should be noted that the hump onset near 2500 cm^{-1} was observed in reflectance measurements by Langhammer et al. Figure 5.12 [19]. This weak feature is probably an indirect transition. The higher the doping concentration of impurities in Sb_2Te_3, the less prominent this feature is, since the degree of disorder increases with doping concentration of impurities. Hence in Figure 5.11, the observed feature is best seen in Sb_2Te_3 and least distinct in $Sb_{1.94}Cr_{0.06}Te_3$.
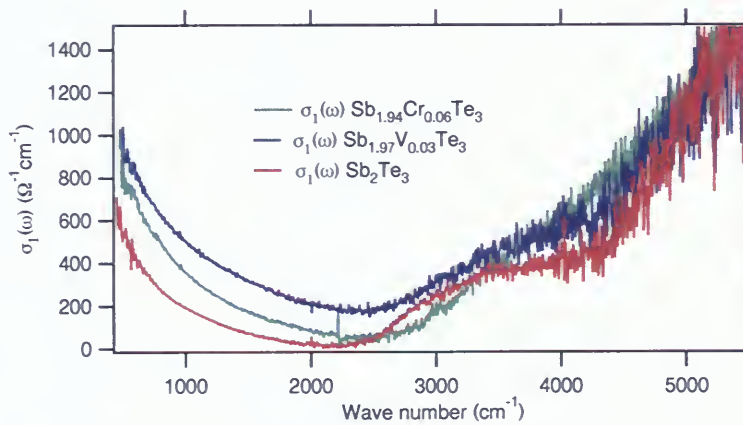
Figure 5.11: Real part of the conductivity spectra for Sb_2Te_3, $Sb_{1.94}Cr_{0.06}Te_3$ and $Sb_{1.97}V_{0.03}Te_3$ at 295K obtain after KK analysis of the samples. In each spectrum, a hump that is probably associated with an indirect transition can be observed between $2000cm^{-1}$ and $3000cm^{-1}$.

The FIR spectra of real conductivity for $Sb_{1.94}Cr_{0.06}Te_3$ and $Sb_{1.97}V_{0.03}Te_3$ at four different temperatures are shown in Figures 5.13 and 5.14 respectively. Peaks associated with
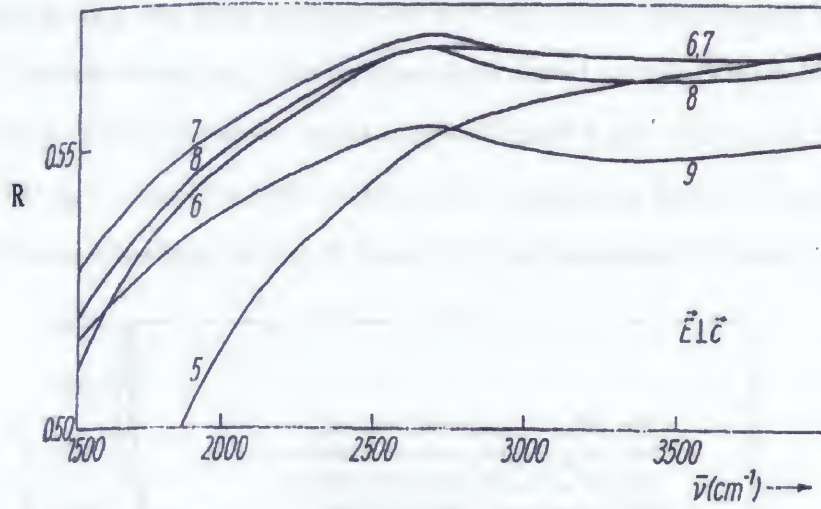
Figure 5.12: Reflectivity R spectrum from 1500-4000cm^{-1} measured by Langhammer et al. The numbers 5-9 represent different treatment given to Sb$_2$Te$_3$ during the growth process. (5) +0.1 at% lead, 14 days growth process; (6) +0.2 at% iodine, 14 days growth process; (7) +5 at% tellurium, 10 days growth process; (8) +5 at% tellurium, 14 days growth process. The electric field is perpendicular to c axis (E⊥c). A hump could be observed between 2500cm^{-1} and 3000cm^{-1} for the samples labelled 7, 8 and 9 [19].
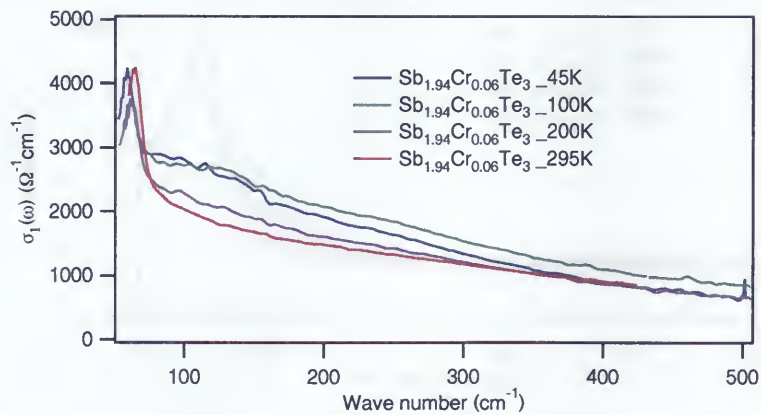
Figure 5.13: Real conductivity spectra $\sigma_1(\omega)$ of Sb$_{1.94}$Cr$_{0.06}$Te$_3$ at 45K, 100K, 200K and 295K.

phonons are seen below 100cm^{-1}. These peaks move towards lower wave number with decreasing temperature (phonon softening). The spectra fall off sharply after the peaks but do not form minimum dips and tend to somewhat converge before approaching the frequency of 500cm^{-1}. The features in $\sigma_1(\omega)$ for the vanadium doped sample (Figure 5.14) are more distinct than those of the chromium doped sample (Figure 5.13). This could be due to the fact that the chromium doped sample contains more impurities than the vanadium doped sample. The phonon softening features of Figure 5.14 are prominently shown in Figure 5.15.
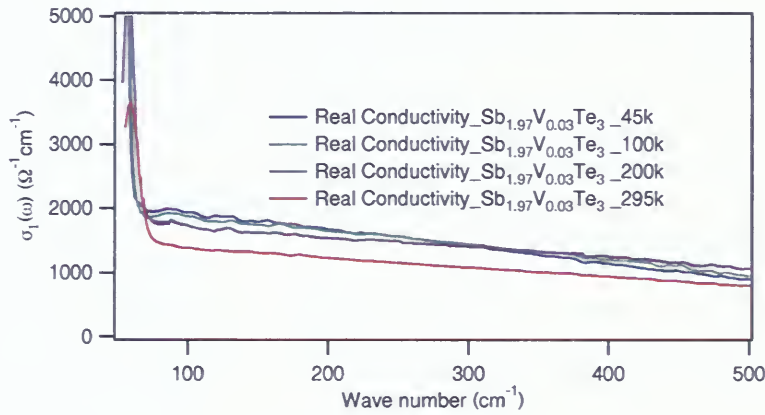
Figure 5.14: $\sigma_1(\omega)$ of $Sb_{1.97}V_{0.03}Te_3$ obtained by KK analysis described in the text.
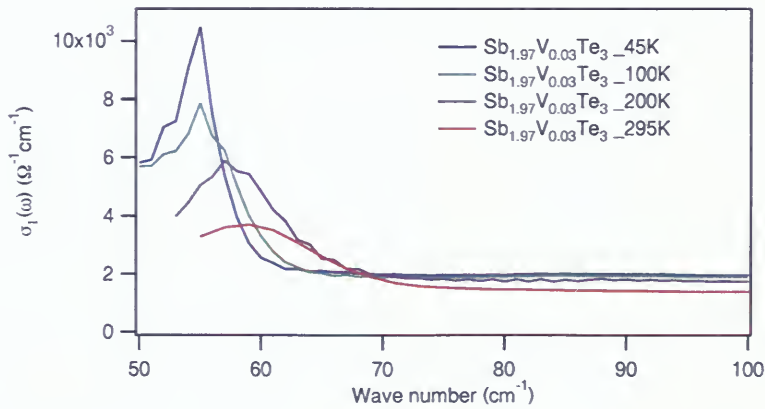
Figure 5.15: Phonon softening features of Figure 5.14.

The parameters found in the Drude-Lorentz model fits (Tables 5.1 and 5.2) can be used to obtain $\sigma_1(\omega)$ by KK analysis of the samples (Figure 5.16). The doped samples of Sb_2Te_3 behave like conventional metals since they closely follow the Drude-Lorentz model. It should
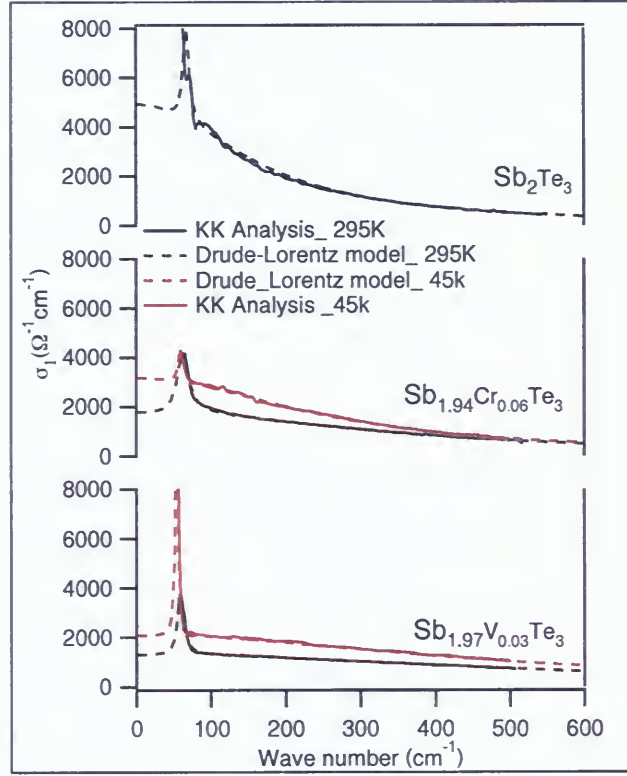
Figure 5.16: Drude-Lorentz fit of σ_1 obtained from KK analysis of the samples used in this work at 45K and 295K.

be noted that materials like superconductors are not conventional metals. Temperature dependence of the scattering rate is shown in Figure 5.17. The concentration of impurities in the chromium doped sample are more than those in the vanadium doped sample, yet the scattering rate of the vanadium doped sample is more than that of the chromium doped sample (Figure 5.17). The reason may be that the scattering cross section of the vanadium impurities is larger than that of the chromium impurities. Note that there are two different Te sites in the crystal structure shown in Figure 1.2. Perhaps V preferentially substitute close to one of these Te sites whereas Cr does not causing increased scattering for the V

doped sample.
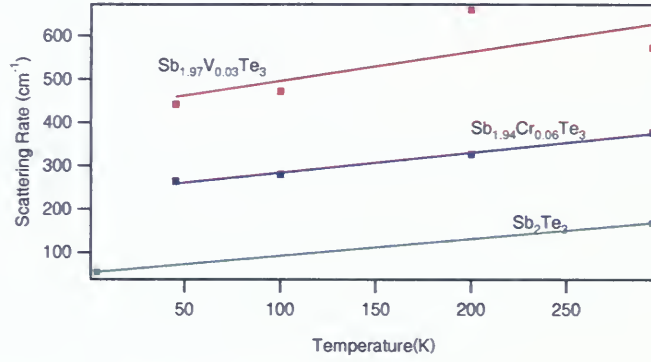
Figure 5.17: Temperature dependence of the scattering rate for $Sb_{1.97}V_{0.03}Te_3$, $Sb_{1.94}Cr_{0.06}Te_3$ and Sb_2Te_3

The feature of $Sb_{1.97}V_{0.03}Te_3$ shown in Figure 5.15 that we are curious about is the fact that the oscillator strength (area of phonon peak) of the phonon increases as T decreases. This can also be seen in Table 5.2. On the other hand, the oscillator strength of the phonon in $Sb_{1.94}Cr_{0.06}Te_3$ decreases as temperature decreases. Also, the curvature of $\sigma_1(\omega)$ for the Cr doped sample at 295K (Figure 5.13) changes from concave-up to concave-down near $150cm^{-1}$. At this point, the origin of this difference in behaviour between the Cr and V doped samples is unclear.

Chapter 6

Conclusions

The direct current resistivities of the samples were measured between the temperatures of 4K and 300K. The result of these resistivity measurements showed that the data for Sb_2Te_3 is in agreement with a previous experiment [3, 4] while that of $Sb_{1.94}Cr_{0.06}Te_3$ and $Sb_{1.97}V_{0.03}Te_3$ differ, though the trend of the results with temperature is similar for both experiments. The inhomogeneity of the distribution of Cr and V across the sample layers and the fact that many of the surface layers of the samples have been removed in a bid to have clean surfaces for the experiments could account for the disagreement of the resistivity results.

The far infrared optical properties of Sb_2Te_3, $Sb_{1.97}V_{0.03}Te_3$ and $Sb_{1.94}Cr_{0.06}Te_3$ were studied near normal incidence at different temperatures (between 45K and 300K). Also Kramers Kronig analysis was performed on the reflectance spectra to obtain the optical conductivities. In the doped samples, it was observed that a phonon at $62cm^{-1}$ softens to about $55cm^{-1}$ on decreasing the temperature from 295K to 45K. Also, it was observed that the plasma frequency of the doped samples is almost independent of doping.

The scattering rate for the vanadium doped sample was seen to be greater than that for the chromium doped sample despite the fact that the vanadium impurity density is less than that of chromium . One can suggest that vanadium has a larger scattering cross section than chromium. The Drude-Lorentz model fits the KK optical conductivity well. This suggests that the samples used in this work behave like normal metals.

Definitive measurements of the temperature dependence of the scattering rate across the ferromagnetic transition await equipment changes enabling low temperature measurements using the MCT detector. The MCT in our laboratory should be fixed because it leaks,

causing absorption at 3200cm^{-1} due to ice formation. It is important to try to attain lower temperature in the new system. This may be achieved by using the radiation shield and more copper braids to connect the Janis to the sample.

Appendix A

A.1 Lorentz Oscillator Model

This model can be used for either infrared active phonons or interband transitions. One assumes that the external electromagnetic wave couples to a dipole modelled by a damped harmonic oscillator since oscillating dipoles may lose energy by coupling to enviroment. Under the influence of an electric field, the equation of motion for this model is given by [9]:

$$m\frac{d^2r}{dt^2} + m\Gamma\frac{dr}{dt} + m\omega_0^2 r = -eE \tag{A.1}$$

where m is the mass of the spring, the first term on the left is Newton's force (i.e. inertia term), the second term represents a frictional force with damping (Γ is the damping term). $\Gamma = \frac{1}{\tau}$, where τ is the scatttering time. The third term on the left is the Hooke's law restoring force, where ω_o is the resonance frequency, given as

$$\omega_o = \sqrt{\frac{k}{\mu}}, \tag{A.2}$$

k is the force constant, and μ is the reduced mass of the system. For interband transitions, $\hbar\omega_0$ is the energy gap while for phonons, ω_0 is the phonon frequency at the center of the brillouin zone. The term on the right hand side of equation(A.1) is the driving force, e is the magnitude of the electronic charge and E is the local electric field that drives the electron. Assuming that the local electric field E and displacement from the equilibrium position r have a time dependence of the form $exp(-i\omega t)$, then the solution to equation(A.1)becomes

$$r = \frac{-eE/m}{(\omega_0^2 - \omega^2) - i\Gamma\omega}. \tag{A.3}$$

The induced dipole moment is p=-er; combining with equation(A.3), it becomes

$$p = \frac{e^2 E}{m}\frac{1}{(\omega_0^2 - \omega^2) - i\Gamma\omega}. \tag{A.4}$$
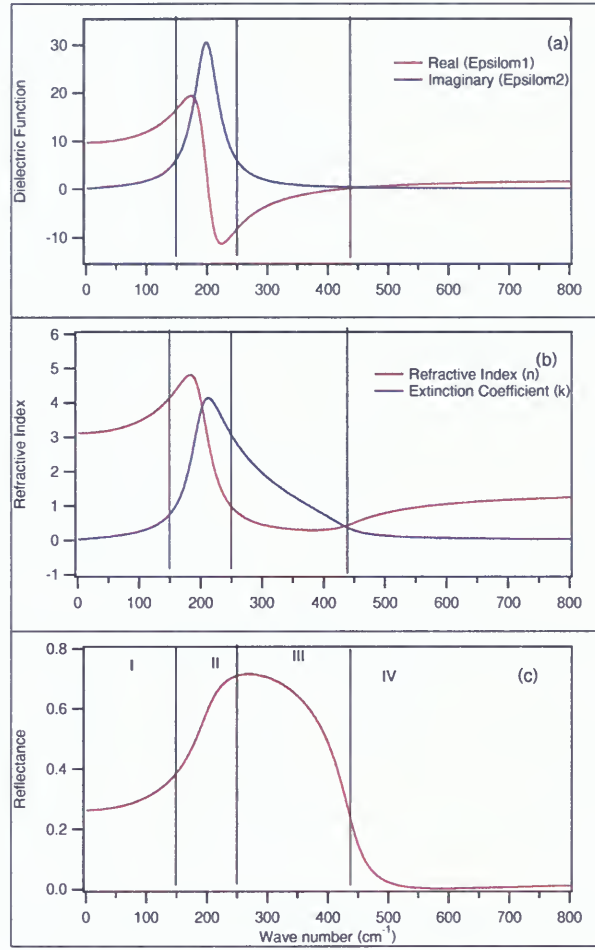
Figure A.1: (a) Real and imaginary parts of the dielectric function,(b) Real and Imaginary parts of the refractive index and (c) reflectance plotted as a function of wavenumber(cm^{-1}),calculated for ω_0=200cm^{-1}, ω_p=550cm^{-1}, Γ=50cm^{-1}. The four regions (regions I,II,III,IV) are also well shown in the graph.

Suppose the displacement r is very small, then,

$$p = \alpha(\omega)E \tag{A.5}$$

where $\alpha(\omega)$is atom polarizability. Comparing equations (A.4) and (A.5), one obtains

$$\alpha(\omega) = \frac{e^2}{m}\frac{1}{(\omega_0^2 - \omega^2) - i\Gamma\omega}. \tag{A.6}$$

Equation(A.6) is the polarizability for a single dipole. The macroscopic polarizability(assuming that each atom contributes just one electron to the absorption process) [7] is

$$P = Np = N\alpha(\omega)E = N\frac{e^2}{m}\frac{1}{(\omega_0^2 - \omega^2) - i\Gamma\omega}E = \chi E \tag{A.7}$$

where χ is the dielectric susceptibility and N is the number of atoms per unit volume. But the relation between dielectric constant and dielectric susceptibility is given by

$$\varepsilon = 1 + 4\pi\chi = 1 + \frac{4\pi Ne^2}{m}\frac{1}{(\omega_0^2 - \omega^2) - i\Gamma\omega}. \tag{A.8}$$

The real part ε_1 and the imaginary part ε_2 of equation (A.8) could be written as

$$\varepsilon_1 = 1 + \frac{4\pi Ne^2}{m}\frac{(\omega_0^2 - \omega^2)}{(\omega_0^2 - \omega^2)^2 + \Gamma^2\omega^2} = n^2 - \kappa^2 \tag{A.9}$$

$$\varepsilon_2 = 1 + \frac{4\pi Ne^2}{m}\frac{\Gamma\omega}{(\omega_0^2 - \omega^2)^2 + \Gamma^2\omega^2} = 2n\kappa \tag{A.10}$$

The real σ_1 and imaginary σ_2 components of the optical electrical conductivity are

$$\sigma_1 = \frac{\omega \times \varepsilon_2}{4\pi} = \frac{Ne^2}{m} \times \frac{\omega^2\Gamma}{(\omega_0^2 - \omega^2)^2 + \Gamma^2\omega^2} \tag{A.11}$$

$$\sigma_2 = \frac{(\varepsilon_1 - 1) \times \omega}{4\pi} = \frac{Ne^2}{m} \times \frac{\omega(\omega_0^2 - \omega^2)}{(\omega_0^2 - \omega^2)^2 + \Gamma^2\omega^2} \tag{A.12}$$

There are four spectral ranges in the Lorentz model (Figure A.1):

Region I

This occurs at low frequency (Figure A.1) , $\omega_0 \gg \omega$, the real part of the conductivity, the imaginary parts of the dielectric function and the refractive index can be neglected since there is little absorption. Hence the reflectivity is given as

$$R = (\frac{1 - \varepsilon_1^{1/2}}{1 + \varepsilon_1^{1/2}})^2 = (\frac{1 - n}{1 + n})^2 \tag{A.13}$$

Region I is known as the transparent region.

Region II

This region $(\omega_0 - \frac{1}{2}\Gamma) < \omega < (\omega_0 + \frac{1}{2}\Gamma)$ is known as the absorption region because there is strong absorption around the oscillator frequency ω_0. This strong absorption is due to the

large conductivity σ_1 [7]. Several optical quantities (i.e reflectivity, refractive index) show strong changes in region II.

Region III

In region III, $\omega \gg \omega_0$, the energy of the incoming light is much greater than the binding energy of the electrons, so electrons in the insulator behave as if they were free electrons. Hence the reflectance of the insulator is like that of a metal [7]. In good insulators it lies in the vacuum-ultraviolet region, while in semiconductors, this region is in the visible.

Region IV

Region IV is known as the transparent regime. It is characterized by $\varepsilon_1 = 0$. This region begins at a characteristic frequency known as plasma frequency ω_p [9]. It is written as

$$\omega_p^2 = \frac{4\pi N e^2}{m}. \tag{A.14}$$

The extinction coefficient here is small hence reflectivity is dominated by the real refractive index n.

A.2   Drude Model

Unlike bound electrons, free electrons do not experience a restoring force when they interact with light, hence $\omega_0{=}0$. Equation(A.1) then becomes

$$m\frac{d^2 r}{dt^2} + m\Gamma\frac{dr}{dt} = -eE. \tag{A.15}$$

Equations(A.9) and (A.10) then becomes

$$\varepsilon_1 = 1 - \frac{\omega_p^2}{\Gamma^2(1+\frac{\omega^2}{\Gamma^2})} = 1 - \frac{4\pi N e^2}{m}\frac{1}{(\omega^2+\Gamma^2)} = n^2 - \kappa^2, \tag{A.16}$$

$$\varepsilon_2 = \frac{\omega_p^2}{\omega\Gamma(1+\frac{\omega^2}{\Gamma^2})} = \frac{4\pi N e^2}{m}\frac{\Gamma}{\omega(\omega^2+\Gamma^2)} = 2n\kappa. \tag{A.17}$$

Some regimes can be distinguished in the Drude model:

Hagen-Ruben's Regime

This region occurs at low frequency and is characterized by $\omega \ll \Gamma$. The equations for dielectric constant, refractive index and reflectivity become
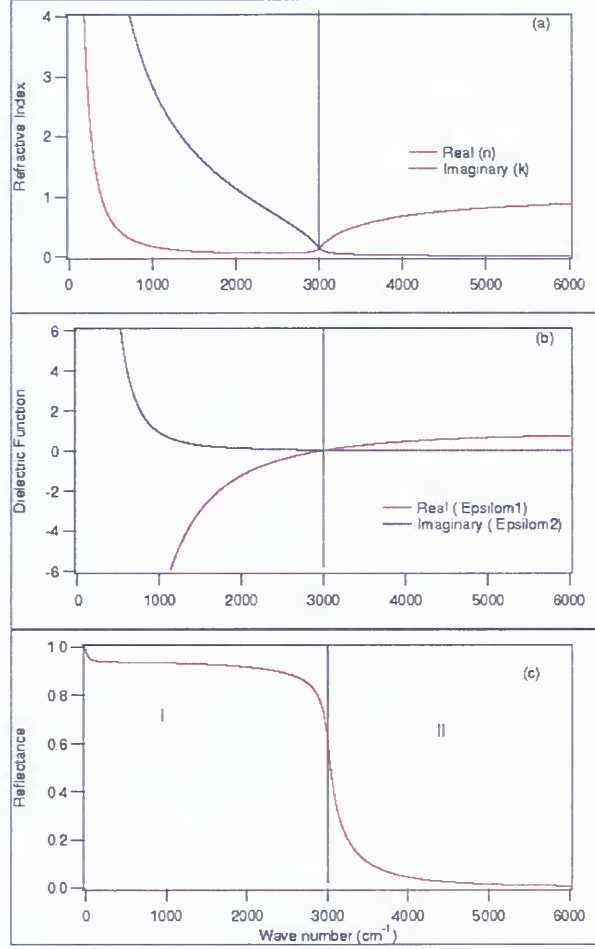
Figure A.2: (a) Dielectric function, (b) refractive index, and (c) reflectance as a function of wavenumber (cm^{-1}), $\omega_p = 3000 cm^{-1}$ and $\Gamma = 100 cm^{-1}$. In the graph, region I is the relaxation region while region II is the transparent region.

$$\varepsilon_1 \approx -\frac{\omega_p^2}{\Gamma^2} \tag{A.18}$$

$$\varepsilon_2 \approx \frac{\omega_p^2}{\omega\Gamma} = \frac{4\pi\sigma_{dc}}{\omega} \tag{A.19}$$

where σ_{dc} is the dc electrical conductivity

$$n \approx \kappa \approx (\frac{\varepsilon_2}{2})^{1/2}, \tag{A.20}$$

$$R = 1 - \frac{2}{n} = 1 - (\frac{2\omega}{\pi\sigma_{dc}})^{1/2}. \tag{A.21}$$

The real part of the dielectric constant is large and negative, the imaginary part is positive and larger than the real part. The real part of the refractive index is high, giving a reflectivity of about one hundred percent.

Relaxation regime

This regime lies in the frequency range $\Gamma < \omega < \omega_p$, ε_1 is negative and much greater than ε_2, $\kappa \gg$ n and the reflectivity is still around one hundred percent (This region is represented in Figure A.2 as region I).

Transparent Regime

A metal becomes transparent beyond the plasma frequency ω_p (Figure A.2) (the regime is represented as region II). Hence the transparent regime is characterized by $\omega > \omega_p$. The relation between the conductivity and the frequency can be written as

$$\sigma_1(\omega) \propto \frac{1}{\omega^2}, \tag{A.22}$$

$$\sigma_2(\omega) \propto \frac{1}{\omega}. \tag{A.23}$$

Bibliography

[1] S. A. Wolf, D. D. Awschalom, R. A. Buhrman, J. M. Daughton, S. von. Molnár, M. L. Roukes, A. Y. Chtchelkanova, D. M. Treger, "Spintronics:A Spin-Based Electronic Vision for the Future" Science Magazine **294**, 1488(2001).

[2] J. R. Simpson, H. D. Drew, S. R. Shinde, R. J. Choudhary, S. B. Ogale, T. Venkatesan, "Optical band-edge shift of anatase $Ti_{1-x}Co_xO_{2-\delta}$" Phys. Rev.B **69**, 193205(2004).

[3] J. S. Dyck, P. Hájek, P. Lošt'ák, C. Uher, "Dilute magnetic semiconductors based on $Sb_{2-x}V_xTe_3$" Phys. Rev.B **65**, 115212(2002).

[4] J. S. Dyck, Č. Drasšar, P. Lošt'ák, C. Uher, "Low-temperature ferromagnetic properties of the dilute magnetic semiconductor $Sb_{2-x}Cr_xTe_3$" Phys. Rev.B **71**, 115214(2005).

[5] T. Thonhauser, G. S. Jeon, G. D. Mahan, J. O. Sofo, "Stress-induced defects in Sb_2Te_3" Phys. Rev.B **68**, 205207(2003).

[6] P. Lošt'ák, Č. Drašar, J. Navráth, L. Beneš, "Sb_2Te_3 Single Crystals doped with Chromium Atoms" Cryst. Res. Technol.**31**, 403-413(1996).

[7] M. Dressel, G. Grüner, *Electrodynamics of Solids* (Cambridge University Press, Cambridge, U.K., 2002).

[8] M. Fox, *Optical Properties of Solids* (Oxford University Press, Oxford, U.K., 2001).

[9] F. Wooten, *Optical Properties of Solids* (Academic Press, New York, U.S.A., 1972).

[10] H. Köhler, C. R. Becker, "Optically Active Lattice Vibrations in Bi_2Se_3" Phys. Stat. sol.(b) **61**, 533(1974).

[11] W. Richter, H. Köhler, C. R. Becker, "A Raman and Far-Infrared Investigations of Phonons in the Rhombohedral V_2-VI_3 Compounds" Phys. Stat. sol.(b) **84**, 619(1977).

[12] D. L. Greenaway, G. Harbeke, "Band Structure of Bismuth Telluride, Bismuth Selenide and their respective alloys" J.Phys.Chem.Solids **26**, 1585-1604(1965).

[13] G. A. Thomas, D. H. Rapkine, R. B. Van. Dover, L. F. Mattheiss, W. A. Sunder, L. F. Schneemeyer, "Large electronic-density increase on cooling a layered metal: Doped Bi_2Te_3" Phys. Rev.B **46**, 1553(1992).

[14] http://electron.mit.edu/ gsteele/vanderpauw

[15] S. Ocadlik, " Far infrared spectroscopy of heavy fermion superconductor CeCoIn5" Brock University, St.Catharines(2004).

[16] J. R. Klassen, "The design of a reflectance spectrometer and its calibration using $SrTiO_3$" Brock University, St.Catharines(2004).

[17] B. Liu, "Optical properties of organic superconductor $\kappa - (BETS)_2 FeBr_4$" Brock University, St.Catharines(2007).

[18] L. Rozema, "Room Temperature Optical Properties of Dilute Magnetic Semiconductors $Sb_{1.97}V_{0.03}Te_3$ and $Sb_{1.94}Cr_{0.06}Te_3$" PHYS 4F90, Brock University, St.Catharines(2007).

[19] H. T. Langhammer, M. Stordeur, H. Sobotta, V. Riede, "Optical and Electrical Investigations of the Anisotropy of Sb_2Te_3 Single Crystals" Phys. Stat. sol.(b) **109**, 673(1982).